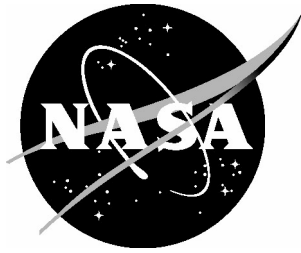# Evaluation of a Multigrid Scheme for the Incompressible Navier-Stokes Equations

R. C. Swanson
Langley Research Center, Hampton, Virginia

Since its founding, NASA has been dedicated to the advancement of aeronautics and space science. The NASA Scientific and Technical Information (STI) Program Office plays a key part in helping NASA maintain this important role.

The NASA STI Program Office is operated by Langley Research Center, the lead center for NASA's scientific and technical information. The NASA STI Program Office provides access to the NASA STI Database, the largest collection of aeronautical and space science STI in the world. The Program Office is also NASA's institutional mechanism for disseminating the results of its research and development activities. These results are published by NASA in the NASA STI Report Series, which includes the following report types:

- TECHNICAL PUBLICATION. Reports of completed research or a major significant phase of research that present the results of NASA programs and include extensive data or theoretical analysis. Includes compilations of significant scientific and technical data and information deemed to be of continuing reference value. NASA counterpart of peer-reviewed formal professional papers, but having less stringent limitations on manuscript length and extent of graphic presentations.

- TECHNICAL MEMORANDUM. Scientific and technical findings that are preliminary or of specialized interest, e.g., quick release reports, working papers, and bibliographies that contain minimal annotation. Does not contain extensive analysis.

- CONTRACTOR REPORT. Scientific and technical findings by NASA-sponsored contractors and grantees.
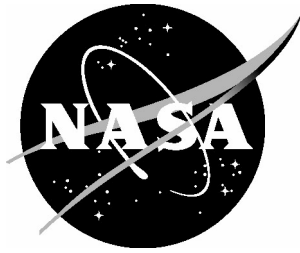
- CONFERENCE PUBLICATION. Collected papers from scientific and technical conferences, symposia, seminars, or other meetings sponsored or co-sponsored by NASA.

- SPECIAL PUBLICATION. Scientific, technical, or historical information from NASA programs, projects, and missions, often concerned with subjects having substantial public interest.

- TECHNICAL TRANSLATION. English-language translations of foreign scientific and technical material pertinent to NASA's mission.

Specialized services that complement the STI Program Office's diverse offerings include creating custom thesauri, building customized databases, organizing and publishing research results ... even providing videos.

For more information about the NASA STI Program Office, see the following:

- Access the NASA STI Program Home Page at *http://www.sti.nasa.gov*

- E-mail your question via the Internet to help@sti.nasa.gov

- Fax your question to the NASA STI Help Desk at (301) 621-0134

- Phone the NASA STI Help Desk at (301) 621-0390

- Write to:
  NASA STI Help Desk
  NASA Center for AeroSpace Information
  7121 Standard Drive
  Hanover, MD 21076-1320

Evaluation of a Multigrid Scheme for the Incompressible Navier-Stokes Equations

R. C. Swanson
Langley Research Center, Hampton, Virginia

May 2004

Available from:

Contents

ABSTRACT

A fast multigrid solver for the steady, incompressible Navier-Stokes equations is presented. The multigrid solver is based upon a factorizable discrete scheme for the velocity-pressure form of the Navier-Stokes equations. This scheme correctly distinguishes between the advection-diffusion and elliptic parts of the operator, allowing efficient smoothers to be constructed. To evaluate the multigrid algorithm, solutions are computed for flow over a flat plate, parabola, and a Kármán-Trefftz airfoil. Both nonlifting and lifting airfoil flows are considered, with a Reynolds number range of 200 to 800. Convergence and accuracy of the algorithm are discussed. Using Gauss-Seidel line relaxation in alternating directions, multigrid convergence behavior approaching that of $O(N)$ methods is achieved. The computational efficiency of the numerical scheme is compared with that of Runge-Kutta and implicit upwind based multigrid methods.

1   INTRODUCTION

One of the critical needs in computational fluid dynamics is faster flow solvers. Multigrid is a well known method of convergence acceleration that is widely used in Euler and Reynolds-averaged Navier-Stokes codes. These applications of multigrid generally are based on the unsteady equations using some temporal integrator as the smoother, combined with a full-approximation scheme (FAS) multigrid iteration. A common approach is one originally proposed by Jameson [1]. Starting with the unsteady equations, a finite-volume spatial discretization with explicit artificial viscosity is combined with a Runge-Kutta (R-K) time integration as a smoother. An alternative approach [2, 3, 4] is to use upwind-differencing and implicit time integration as the smoother. However, these approaches have resulted in poor multigrid efficiency. When applied to high Reynolds number flows over complex geometries, convergence rates are often worse than 0.99. There is clearly a need to develop substantially more efficient multigrid solvers.

According to Brandt [7], one of the major obstacles to achieving better multigrid performance for advection dominated flows is that the coarse grid provides only a fraction of the needed correction for some smooth error components. This obstacle can be removed by designing a solver that effectively distinguishes between the advection and elliptic (hyperbolic if Mach number exceeds one) factors of the system and treats each one appropriately. For instance, advection can be treated by space marching, while elliptic factors can be treated by multigrid. The efficiency of such an algorithm will be essentially identical to that of the solver for the elliptic factor only, and thereby attain so-called "textbook" multigrid efficiency. Such efficiency can also be viewed as the efficiency that can be attained when solving a pure elliptic problem (e.g., Poisson equation).

One essential element for achieving textbook multigrid efficiency is an effective multigrid scheme. The performance of a multigrid scheme strongly depends upon two components: 1) relaxation (smoother), 2) coarse-grid operator. A relaxation process is devised such that it effectively smooths, as determined by its smoothing factor, the high-frequency components of the solution error, and a coarse-grid operator is designed so that it efficiently reduces the low-frequency error components. Generally, a smoothing factor of 0.5 is considered good. Such a scheme is said to have a good measure of h-ellipticity. Often, the amenability of a discrete operator to a multigrid algorithm is characterized by the h-ellipticity of the operator. For the purpose of subsequent discussion the definiton of h-ellipticity is given here. The measure of h-ellipticity is defined in the following way (see discussion in Trottenberg, Oosterlee, and Schüller [5]). Let $\mathbf{L}_h$ represent the discrete operator matrix for the system of equations on a discrete domain with uniform spacing h. Also, let E_h be the measure of h-ellipticity. Then,

$$E_h(\mathbf{L}_h) \equiv \frac{\min\left\{|\det \hat{\mathbf{L}}_h(\theta_x, \theta_y)| : \frac{\pi}{2} \le |\theta_x|, |\theta_y| \le \pi\right\}}{\max\left\{|\det \hat{\mathbf{L}}_h(\theta_x, \theta_y)| : 0 \le |\theta_x|, |\theta_y| \le \pi\right\}},$$

where $\hat{\mathbf{L}}_h$ is the Fourier symbol of the operator $\mathbf{L}_h$, and θ_x, θ_y are proportional to the wave numbers associated with the x and y coordinate directions, respectively. According to this definition, good h-ellipticity means that E_h must be bounded away from zero by a suitable constant. As a reference, a standard five-point discretization of the Laplacian has an E_h of 0.25. To achieve textbook multigrid efficiency, the discrete operators of the multigrid algorithm must have good h-ellipticity.

Another essential element for attaining textbook multigrid efficiency is factorizability. A scheme is defined to be factorizable if the determinant of the discrete operator matrix can be represented as the product of separate scalar factors (e.g., advection-diffusion, elliptic). With a factorizable scheme the solution to the system is reduced to the solution of the separate scalar factors. The key

aspect of the factorization is that only those terms that contribute strongly to the high-frequency components of the error must be considered when constructing the relaxation method. These terms are called the "principal part" of the operator. The approach advocated by Brandt is to introduce a transformation of the dependent variables to a set of auxiliary variables, which he calls "ghost" variables, such that the principal part of the operator is triangular. The equation residuals produce increments in the ghost variables, which are distributed to the primary variables by means of the transformation (distribution) matrix. This is called "distributive relaxation" (for further discussion see Brandt [7], Hackbush [6], Trottenberg et al. [5]). An alternative to distributive relaxation is to find a projection matrix for the original system such that the principal part of the resulting discrete system is in triangular form, but in terms of the orignal set of dependent variables. This is the approach used here.

Relatively little research has been done in the area of multigrid algorithms for the Navier-Stokes equations based upon factorizable discrete schemes. Using a scheme based on distributive relaxation, Brandt and Yavneh [8] have demonstrated textbook multigrid efficiency for the incompressible Navier-Stokes equations for entering flow. Their results are for a simple geometry and a Cartesian grid, using a staggered-grid discretization (i.e., velocity components and pressure stored at different locations) of the equations.

Recently, Thomas, Diskin, and Brandt[9] achieved textbook multigrid efficiency for high Reynolds number incompressible wake and boundary layer flows associated with a flat plate. Their scheme uses a staggered grid approach with distributed relaxation and defect correction. With the distributive relaxation the system of equations was decomposed (i.e., factorized) everywhere, except near boundaries where they remained coupled. In all calculations Cartesian grids were used.

Sidilkover and Asher[10] introduced a fast multigrid solver for the incompressible Navier-Stokes equations that does not require a staggered grid arrangement of flow variables. With a pressure Poisson formulation as a foundation, a factorizable discrete scheme is derived. In this work also only simple model problems were solved using uniform Cartesian grids.

In this paper a generalization of the approach of Sidilkover and Ascher[10], which is a continuation of the work of Roberts and Swanson [11] and Swanson [12], is used. A conventional vertex-based finite-volume or finite-difference discretization of the primitive variables is used, avoiding the need for staggered grids. This simplifies the restriction and prolongation operations, because the same operator can be used for all variables. A projection operator is applied to the incompressible Navier-Stokes equations in velocity-divergence form to obtain a factorizable discrete scheme with decoupling for the velocity-pressure form of the Navier-Stokes equations, except near the boundaries of the domain being considered. For the pressure equation a numerical a boundary condition based on the momentum equations is introduced to enforce continuity at the inflow and solid surface boundaries. Gauss-Seidel relaxation is used as a smoother of the Poisson equation for the pressure. The momentum equations are relaxed by space marching. Since the elliptic and advection-diffusion parts of the system are decoupled over most of the flow field, ideal multigrid efficiency is possible. With the present scheme line relaxation is used to treat the anisotropy of mesh aspect ratio that generally occurs in resolving viscous flows.

The primary purpose of this paper is to evaluate a modified version of the scheme introduced by Swanson [12], herein called INCOMP scheme. In Section 2 the governing equations are presented. An iterative operator matrix is determined by applying a projection matrix. Discretization of the flow equations and the associated boundary conditions are discussed in Sections 3 and 4. Section 5 describes the multigrid algorithm for solving the equations. Then, in Section 6 there is discussion about computation of skin-friction drag. Surface skin friction is as an important quantity in assessing a viscous flow solver. Next, computed results for three types of flows are shown and

2

discussed in Section 7. Flow solutions were calculated for the following geometries: 1) flat plate, 2) parabola, 3) airfoil. Both accuracy and convergence behavior are considered in evaluating the present scheme. The computational work required by the INCOMP scheme is compared to that needed by R-K and implicit upwind multigrid solvers. Concluding remarks are made in Section 8.

2 MATHEMATICAL FORMULATION

The boundary-value problem for the two-dimensional incompressible Navier-Stokes equations can be written as

$$
\begin{aligned}
(\mathbf{V} \cdot \nabla)\mathbf{V} + \nabla p - \nu \Delta \mathbf{V} &= \mathbf{f}, & \mathbf{x} \in \Omega \\
\nabla \cdot \mathbf{V} &= 0, & \mathbf{x} \in \Omega \\
B(\mathbf{V}, p) &= \mathbf{0}, & \mathbf{x} \in \partial\Omega
\end{aligned}
\tag{1}
$$

where $\mathbf{V} = \mathbf{V}(x, y) = (u, v)^T$ is the fluid velocity, $p = p(x, y)$ is the pressure, and Δ is the Laplacian operator. The density is taken to be one, and the coefficient ν is the reciprocal of the Reynolds number, $\nu = 1/Re$. The domain Ω is in $\Re^2$, and the boundary of the domain is $\partial\Omega$. There are two boundary conditions, and these are represented by $B(\mathbf{V}, p)$. In Section 4 the boundary conditions will be discussed in detail. Throughout this paper the forcing function $\mathbf{f} = \mathbf{f}(x, y) = \mathbf{0}$. The system of Eq. (1) is sometimes called the velocity-divergence form of the equations.

The velocity-divergence formulation of Eq. (1) can be used with a staggered-grid discretization. However, such a formulation is not appropriate for a collocated-grid discretization when the continuity equation $\nabla \cdot \mathbf{V}$ and pressure gradient ∇p are approximated with central differencing. Under these circumstances spurious modes in the pressure can be produced (i.e., there is a loss of h-ellipticity).

There are alternative forms for the system of Eq. (1) that are amenable to collocated-grid discretization and to a rapidly convergent numerical soluion procedure, such as one based on a muligrid scheme. One of these forms can be derived by taking the divergence of the momentum equation and applying $\nabla \cdot \mathbf{V} = 0$. The resulting system is is called the velocity-pressure (or pressure Poisson) form of the equations, and the associated boundary-value problem is defined by

$$
\begin{aligned}
(\mathbf{V} \cdot \nabla)\mathbf{V} + \nabla p - \nu \Delta \mathbf{V} &= \mathbf{f}, & \mathbf{x} \in \Omega \\
\Delta p + \nabla u \cdot \mathbf{V}_x + \nabla v \cdot \mathbf{V}_y &= \nabla \cdot \mathbf{f}, & \mathbf{x} \in \Omega \\
B(\mathbf{V}, p) &= \mathbf{0}, & \mathbf{x} \in \partial\Omega \\
\nabla \cdot \mathbf{V} &= 0, & \mathbf{x} \in \partial\Omega,
\end{aligned}
\tag{2}
$$

Now, the pressure equation plays the role of the continuity equation in Ω. Since this equation is second order, the system requires an additional boundary condition. By choosing the additional boundary condition to be $\nabla \cdot \mathbf{V} = 0$, one can prove that the velocity-pressure and velocity-divergence formulations are equivalent (see Trottenberg et al. [5]).

The velocity-pressure form of the equations given in Eq. (2) can be derived other ways that can clearly suggest how to construct a fast solution algorithm. One way is to start by defining an advection-diffusion operator

$$
Q_\nu \equiv Q - \nu \Delta,
\tag{3}
$$

where $Q = u\partial_x + v\partial_y$, and ∂_x, ∂_y are the partial differentiation operators. Equation (1) can then

be written as

$$L\mathbf{q} = \begin{pmatrix} Q_\nu & 0 & \partial_x \\ 0 & Q_\nu & \partial_y \\ \partial_x & \partial_y & 0 \end{pmatrix} \begin{pmatrix} u \\ v \\ p \end{pmatrix} = 0. \tag{4}$$

Next define the operator $\widetilde{Q}_\nu$ according to

$$\widetilde{Q}_\nu(f) \equiv Q^*(f) + \Delta(\nu f) = -\partial_x(uf) - \partial_y(vf) + \Delta(\nu f), \tag{5}$$

where Q^* is the adjoint of Q, and construct a projection operator P as

$$P = \begin{pmatrix} 1 & 0 & 0 \\ 0 & 1 & 0 \\ \partial_x & \partial_y & \widetilde{Q}_\nu \end{pmatrix}. \tag{6}$$

After applying the projection operator to the velocity-divergence form of Eq. (1), which is equivalent to taking the divergence of the momentum equation and applying $\nabla \cdot \mathbf{V} = 0$, one obtains

$$PL\mathbf{q} = \begin{pmatrix} Q_\nu & 0 & \partial_x \\ 0 & Q_\nu & \partial_y \\ 0 & 0 & \Delta \end{pmatrix} \begin{pmatrix} u \\ v \\ p \end{pmatrix} - \mathbf{b} = 0, \tag{7}$$

or

$$\widetilde{L}\mathbf{q} = \mathbf{b} \tag{8}$$

where $\mathbf{b} = \begin{pmatrix} 0 & 0 & b_3 \end{pmatrix}^T$ and

$$b_3 = -\partial_x(vu_y - uv_y) - \partial_y(uv_x - vu_x) \tag{9}$$

The 3×3 upper triangular operator matrix of Eq. (7) corresponds to the operator obtained by linearizing the velocity-pressure form of the system and retaining only principal terms. The principal terms are those that dominate with respect to high-frequency error components. The column vector $\mathbf{b}$ is comprised only of subprincipal terms over most of the domain, and these terms are not important for the purpose of constructing a relaxation scheme.

3   DISCRETIZATION

The first step in approximating $\widetilde{L}$ is to discretize the Navier-Stokes equations given in Eq. (4). Consider a typical grid vertex (i, j) as shown in Fig. 1. The equations are discretized with a combination of finite-difference and finite-volume techniques. For the momentum equations second-order accurate upwind differencing is used for the advection part of the operator Q_ν in Eq. (3). Central differencing is used for the physical diffusion contribution to Q_ν and the pressure gradient term. Discretization of the pressure equation in Eq. (7) is also based on central differencing.

Consider the discretization of the advection term Qu in the x-momentum equation. On a Cartesian grid the second-order upwind-difference discretization of the contributions to Qu is

$$u\partial_x^h u|_{i,j} = \frac{1}{2h} s_u |u_{i,j}| (3 - 4E_x^{-s_u} + E_x^{-2s_u}) u_{i,j},$$
$$v\partial_y^h u|_{i,j} = \frac{1}{2h} s_v |v_{i,j}| (3 - 4E_y^{-s_v} + E_y^{-2s_v}) u_{i,j}, \tag{10}$$
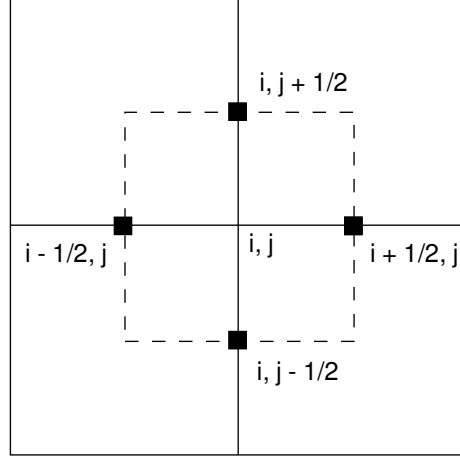
Figure 1: Primary and dual cells on quadrilateral grid.

where the shift operator E is defined by

$$E_x^{-s_u m} u_{i,j} = u_{i-s_u m, j}, \quad E_y^{-s_v m} u_{i,j} = u_{i, j-s_v m}, \tag{11}$$

with $s_u = sign(u_{i,j})$ and $s_v = sign(v_{i,j})$. Here, the superscript h denotes the discrete approximation to the corresponding differential operator. For arbitrary curvilinear coordinates (ξ, η) the advection operator Q is defined by

$$Qu = (u\partial_x + v\partial_y)u = (\bar{U}\partial_\xi + \bar{V}\partial_\eta)u \tag{12}$$

where $\bar{U} = \xi_x u + \xi_y v$ and $\bar{V} = \eta_x u + \eta_y v$ are contravariant velocity components. The transformation from Cartesian coordinates (x, y) to generalized coordinates (ξ, η), which correspond to the (i, j) indices of the grid, is given by

$$\begin{pmatrix} \xi_x & \eta_x \\ \xi_y & \eta_y \end{pmatrix} = J^{-1} \begin{pmatrix} y_\eta & -y_\xi \\ -x_\eta & x_\xi \end{pmatrix}, \tag{13}$$

and the transformation Jacobian $J = x_\xi y_\eta - x_\eta y_\xi$. The terms $\bar{U}\partial_\xi u$ and $\bar{V}\partial_\eta u$ are differenced according to Eq. (10) on a uniform computational space.

To approximate the physical viscous terms in the momentum equations we first compute the gradients of the velocity components at the edges of the dual grid cell, delineated by dashed lines in Fig. 1. The evaluation points are shown as solid squares. For example, the gradients of the velocity component u at the point $(i - 1/2, j)$ of the dual grid cell are

$$u_x = u_\xi \xi_x + u_\eta \eta_x, \qquad u_y = u_\xi \xi_y + u_\eta \eta_y, \tag{14}$$

The derivatives u_ξ and u_η are approximated at the face center by

$$u_\xi|_{i-1/2,j} = u_{i,j} - u_{i-1,j},$$
$$u_\eta|_{i-1/2,j} = \frac{1}{4} \left(u_{i,j+1} + u_{i-1,j+1} - u_{i,j-1} - u_{i-1,j-1} \right), \tag{15}$$

with similar expressions at the points $(i + 1/2, j)$, $(i, j + 1/2)$, and $(i, j - 1/2)$. The gradients of pressure (p) are calculated the same way. The grid metric terms ξ_x, ξ_y, η_x, and η_y are also evaluated on the dual grid face centers.

5

With the velocity gradients known at the faces of the dual grid cell, one can easily approximate the Laplacian in the viscous terms Δu and Δv. Applying Green's theorem to the dual grid cell,

$$\Delta u = \frac{1}{A_{i,j}} \oint_{\partial A_{i,j}} (u_x dy - u_y dx), \qquad \Delta v = \frac{1}{A_{i,j}} \oint_{\partial A_{i,j}} (v_x dy - v_y dx), \tag{16}$$

where $A_{i,j}$ is the area of the dual cell at the vertex (i,j).

The projection operator P is applied to the discrete equations to obtain the residual for the pressure Poisson equation of Eq. (7). In deriving Eq. (7) we assumed that the functions $u(x,y)$ and $v(x,y)$, as well as their spatial derivatives, are continuous in Ω and on $\partial\Omega$. Thus, the order of differentiation does not matter, and the viscous terms are eliminated in the pressure equation. Here, we assume that the discrete operators exhibit this property. Thus we are assuming that the differential equalities

$$\partial_y \, \partial_y \, \partial_x = \partial_x \, \partial_y \, \partial_y, \qquad \partial_x \, \partial_x \, \partial_y = \partial_y \, \partial_x \, \partial_x. \tag{17}$$

have discrete analogs. Letting $(r_p)_{i,j}$ be the pressure equation residual at vertex (i,j), the application of P can be written in integral form,

$$(r_p)_{i,j} = \oint_{\partial A_{i,j}} \left(\boxed{Q^h u + \partial_x^h p} - u \, \boxed{\left(\partial_x^h u + \partial_y^h v \right)} \right) dy - \left(\boxed{Q^h v + \partial_y^h p} - v \, \boxed{\left(\partial_x^h u + \partial_y^h v \right)} \right) dx. \tag{18}$$

The discretization of the pressure equation is done by first discretizing the boxed terms of Eq. (18) on the edges of the dual grid cell. The integral of Eq. (18) is then evaluated to get the pressure equation residual at the vertex (i,j), taking the boxed terms to be constant over each face of the dual grid cell. For a uniform Cartesian grid, the principal part of the resulting discretization is a conventional five-point approximation to the Laplacian operating on the pressure. At inflow and surface boundaries additional terms appear in the residual due to the implementation of the divergence-free boundary condition. These terms will be defined in Section 4 on boundary conditions.

4   BOUNDARY CONDITIONS

For a given physical problem let the domain of interest and its boundary be denoted by Ω and $\partial\Omega$, respectively. Let the boundary be partitioned according to

$$\partial\Omega = \Gamma_{in} + \Gamma_{out} + \Gamma_{surf}, \tag{19}$$

where Γ_{in} is the inflow part of the boundary, Γ_{out} is the outflow part, and Γ_{surf} is the solid surface part. For each Γ the velocity-pressure formulation of the incompressible N-S equations requires three boundary conditions. The boundary conditions for the velocity-divergence formulation are augmented by an additional boundary condition associated with the pressure equation.

There has been considerable discussion in the literature (e.g., [14] - [18]) regarding the proper boundary condition for the pressure equation. According to Gresho and Sani [14] the normal component of the momentum equation is the appropriate boundary condition. However, as indicated by Henshaw [15], this particular boundary condition allows a nonzero divergence on the boundary, and thus, allows a nonzero divergence in the domain Ω. Furthermore, Strikwerda [17] points out that this boundary condition provides no new information, resulting in an underdetermined system. The viewpoint adopted here is that $\nabla \cdot \mathbf{V} = 0$ is the proper boundary condition. With $\nabla \cdot \mathbf{V} = 0$ on

the boundary $\partial\Omega$ and sufficiently smooth solutions, the velocity-divergence and velocity-pressure formulations are equivalent. This leads to a well-posed problem. The momentum equation provides a suitable vehicle for implementing this boundary condition in the discrete problem.

The boundary conditions along the boundary $\partial\Omega$ are specified according to

$$u(x,y) = u_{in}(x,y), \quad v(x,y) = v_{in}(x,y) \quad \text{on} \quad \Gamma_{in} \tag{20}$$

$$\mathbf{V} \cdot \mathbf{t} = V_t(x,y), \quad p(x,y) = p_{out}(x,y) \quad \text{on} \quad \Gamma_{out} \tag{21}$$

$$u(x,y) = 0, \quad v(x,y) = 0 \quad \text{on} \quad \Gamma_{surf} \tag{22}$$

$$\nabla \cdot \mathbf{V} = 0 \quad \text{on} \quad \partial\Omega \tag{23}$$

where $\mathbf{t}$ is a unit tangent vector and the subscript t means tangential component.

The normal component of the momentum equation can be used to implement the divergence-free boundary condition. Taking the inner product of the unit normal to the boundary and the vector momentum equation, this equation is

$$\frac{\partial p}{\partial n} = -\sum_{j=1}^{2}\sum_{k=1}^{2} n_k V_j \partial_j V_k + \nu \sum_{j=1}^{2}\sum_{k=1}^{2} n_k \partial_j \partial_j V_k, \tag{24}$$

where $V_1 = u$, $V_2 = v$, and the Cartesian components for the inward pointing unit normal to a boundary are $n_1 = n_x$ and $n_2 = n_y$. In the discrete problem the normal pressure gradient of Eq. (24) can be treated as a numerical (Neumann) boundary condition that allows the application of the divergence-free boundary condition $u_x + v_y = 0$.

As discussed previously a finite-volume method is used for the discretization of the pressure equation. At a boundary point (i,j) this method is applied to a half cell, as shown in Fig. 2, surrounding the point. Let Γ_{abcd} be the boundary of the half cell. Along the surface boundary Γ_{ab}
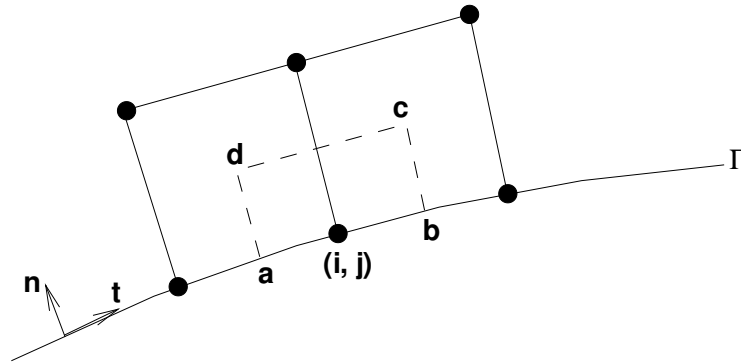

Figure 2: Half cell surrounding boundary point.

the pressure contribution to the integral of Eq. (18) can be expressed as

$$\int_a^b p_x dy - p_y dx = \int_a^b \nabla p \cdot \mathbf{n} ds = \int_a^b \frac{\partial p}{\partial n} ds, \tag{25}$$

where $s = s(x, y)$ is length along the boundary. The normal pressure gradient is given by Eq. (24) with the boundary condition $u_x + v_y = 0$ being imposed. On the boundary Γ_{surf} the normal pressure gradient becomes

$$\begin{aligned}
\frac{\partial p}{\partial n} &= \nu \sum_{j=1}^2 \sum_{k=1}^2 n_k \partial_j \partial_j V_k \\
&= \nu[n_x(u_{xx} + u_{yy}) + n_y(v_{xx} + v_{yy})] \tag{26}
\end{aligned}$$

due to the no-slip condition. The integral of the normal pressure gradient is approximated as

$$\int_a^b \frac{\partial p}{\partial n} ds \approx \left(\frac{\partial p}{\partial n}\right)_{i,j} \Delta s_{ab} = \nu[n_x(u_{xx} + u_{yy})_{i,j} + n_y(v_{xx} + v_{yy})_{i,j}] \Delta s_{ab}, \tag{27}$$

where

$$\begin{aligned}
(u_{xx} + u_{yy})_{i,j} &= A_{1/2}^{-1} \sum_{m=1}^4 (u_x \Delta y - u_y \Delta x)_m, \\
(v_{xx} + v_{yy})_{i,j} &= A_{1/2}^{-1} \sum_{m=1}^4 (v_x \Delta y - v_y \Delta x)_m,
\end{aligned}$$

with $A_{1/2}$ being the half cell area, and in the summations over the four edges of the half cell $u_x = -v_y$ on Γ_{ab}. In the particular case of a flat plate $(y = 0)$ the approximation of Eq. (27) becomes

$$\left(\frac{\partial p}{\partial n}\right)_{i,j} \Delta s_{ab} = \left(\frac{\partial p}{\partial y}\right)_{i,j} \Delta s_{ab} = \nu[(v_y)_{i,j+1/2} - (v_y)_{i,j}] \Delta s_{ab} A_{1/2}^{-1} = \nu(v_y)_{i,j+1/2} \Delta x_{ab} A_{1/2}^{-1}.$$

At the outflow boundary Γ_{out} the x-momentum and y-momentum equations provide numerical boundary conditions for the calculation of the u and v velocity components. The boundary condition $\nabla \cdot \mathbf{V} = 0$ is applied to the physical diffusion terms by substituting $u_x = -v_y$. The streamwise pressure gradient is approximated with second-order one-sided differencing. After updating the pressure along the boundary and solving the system

$$\begin{pmatrix} Q_\nu^h & 0 \\ 0 & Q_\nu^h \end{pmatrix} \begin{pmatrix} \delta u \\ \delta v \end{pmatrix} = \begin{pmatrix} R_u^h \\ R_v^h \end{pmatrix}, \tag{28}$$

the provisional updates $\bar{u}^{l+1}$ and $\bar{v}^{l+1}$ are computed. Then, the solution updates are determined by

$$\begin{pmatrix} u^{l+1} \\ v^{l+1} \end{pmatrix} = \begin{pmatrix} \bar{u}^{l+1} \\ \bar{v}^{l+1} \end{pmatrix} - \begin{pmatrix} t_x \\ t_y \end{pmatrix} [\bar{V}_t^{l+1} - (V_t)_{out}], \tag{29}$$

where t_x and t_y are the Cartesian components of the unit tangent vector to the boundary Γ_{out}.

Suppose we define a sufficiently accurate value of boundary data as one consistent, to the order of approximation, with other data being specified. If a sufficiently accurate value for the tangential

8

velocity $(V_t)_{out}$ at the boundary Γ_{out} is not known, then a significant error in the solution at and near the boundary can be produced. That is, a numerical boundary layer can be created. Such an error can prevent attaining the desired order of accuracy simultaneously in the L_1 and L_2 norms. This behavior was observed at the downstream boundary when computing parabola flows.

An alternative to specifying $(V_t)_{out}$ is to impose the condition that the streamwise physical diffusion associated with the tangential momentum equation is zero. Then, the tangential momentum equation is solved for one velocity component, and the continuity equation is solved for the other velocity component.

5 SOLUTION PROCEDURE

The solution algorithm used for the steady, incompressible Navier-Stokes equations relies upon the factorizability of the corresponding discrete equations. In the present case factorizability necessarily implies a triangular discrete operator matrix. Such a matrix means that the elliptic operator Δ, which is associated with the pressure equation, and the advection-diffusion operator Q_ν can be inverted separately. Rapid inversion, in the sense of operation count, for each of the operators is achieved with a multigrid method. Line Gauss-Seidel relaxation is the smoother for the multigrid process. In the subsequent subsections the relaxation and multigrid schemes are described.

5.1 Relaxation

The relaxation scheme solves for u, v, and p along lines in each coordinate direction. This alternating line relaxation removes the influence of mesh cell aspect ratio on convergence rate. In order to describe the iteration matrix we consider for simplicity a rectangular domain with discrete points defined by $\{(x_{i,j}, y_{i,j}) : 1 \le i \le m, 1 \le j \le n\}$. The iteration matrix for a relaxation sweep with line solves along lines of constant x is defined by

$$
\begin{pmatrix}
B_2 & C_2 & & & & & \\
A_3 & B_3 & C_3 & & & & \\
AA_4 & A_4 & B_4 & C_4 & & & \\
\ddots & \ddots & \ddots & \ddots & & & \\
& AA_{m-3} & A_{m-3} & B_{m-3} & C_{m-3} & & \\
& & AA_{m-2} & A_{m-2} & B_{m-2} & C_{m-2} & \\
& & & AA_{m-1} & A_{m-1} & B_{m-1}
\end{pmatrix}
\begin{pmatrix}
\delta\mathbf{w}_2 \\
\delta\mathbf{w}_3 \\
\delta\mathbf{w}_4 \\
\vdots \\
\delta\mathbf{w}_{m-3} \\
\delta\mathbf{w}_{m-2} \\
\delta\mathbf{w}_{m-1}
\end{pmatrix}
=
\begin{pmatrix}
-\mathbf{R}_2 \\
-\mathbf{R}_3 \\
-\mathbf{R}_4 \\
\vdots \\
-\mathbf{R}_{m-3} \\
-\mathbf{R}_{m-2} \\
-\mathbf{R}_{m-1},
\end{pmatrix}
\tag{30}
$$

where the elements of the change in the solution vector $\delta\mathbf{w}$ and the residual function $\mathbf{R}$ are given by

$$
\delta\mathbf{w}_i = \begin{pmatrix} \delta\mathbf{q}_{i,2} & \delta\mathbf{q}_{i,3} & \cdots & \delta\mathbf{q}_{i,n-2} & \delta\mathbf{q}_{i,n-1} \end{pmatrix}^T, \quad \delta\mathbf{q}_{i,j} = \begin{pmatrix} \delta u_{i,j} & \delta v_{i,j} & \delta p_{i,j} \end{pmatrix}^T,
$$

$$
\mathbf{R}_i = \begin{pmatrix} \mathbf{r}_{i,2} & \mathbf{r}_{i,3} & \cdots & \mathbf{r}_{i,n-2} & \mathbf{r}_{i,n-1} \end{pmatrix}^T, \quad \mathbf{r}_{i,j} = \begin{pmatrix} (r_u)_{i,j} & (r_v)_{i,j} & (r_p)_{i,j} \end{pmatrix}^T
$$

with $i = 2, m-1$ and $j = 2, n-1$. The submatrices AA, A, and C are $(n-2) \times (n-2)$ block diagonal matrices. The B submatrix is a block pentadiagonal matrix, where the diagonal blocks of the submatrices are 3×3 diagonal matrices. All of the other blocks of the submatrices are 3×3 upper triangular matrices. The diagonal elements of the submatrices are the coefficients corresponding to the discrete approximations to the operators Q_ν and Δ. For convenience Eq. (30) can be rewritten as

$$
M\delta\mathbf{w} = -\mathbf{R},
\tag{31}
$$

9

where M is the iteration matrix and

$$\delta\mathbf{w} = \begin{pmatrix} \delta\mathbf{w}_2 & \delta\mathbf{w}_3 & \cdots & \delta\mathbf{w}_{m-2} & \delta\mathbf{w}_{m-1} \end{pmatrix}^T, \quad \mathbf{R} = \begin{pmatrix} \mathbf{R}_2 & \mathbf{R}_3 & \cdots & \mathbf{R}_{m-2} & \mathbf{R}_{m-1} \end{pmatrix}^T.$$

By taking M to be the block lower triangular matrix resulting from ignoring the blocks above the principal diagonal (defined by the B matrices), lexicographic line Gauss-Seidel is obtained with line solves corresponding to lines of constant x. The upper triangular form of the sub-blocks in each of the block matrices of M allows the solution of a tridiagonal system for the pressure on constant x lines followed by the solution of two pentadiagonal systems for the velocity components. Since the velocity on constant x lines is updated using a known pressure, the sequential updating of u and v is equivalent to collective relaxation. In a similar manner the iteration matrix for line solves along lines of constant y can be constructed. This basic part of the relaxation approach does not take into account the coupling between the equations that occurs because of boundary conditions and the stiffness of the equations in the vicinity of solid boundaries. As discussed subsequently the effects of coupling are treated with some additional relaxation at the boundaries.

In numerous practical aerodynamic flows the cross flow physical diffusion dominates the streamwise physical diffusion. If, for such flow problems, upwind differences are used for the advection operator of Eq. (3), then lexicographic line Gauss-Seidel relaxation is essentially equivalent to space marching of the advection terms. The advected error is effectively eliminated in one relaxation sweep and the convergence rate becomes that of the Poisson equation for the pressure. This type of relaxation is sometimes called downstream relaxation. It is possible to get ideal multigrid convergence rates for the system because each component of the error is treated appropriately.

5.2 Multigrid

A sequence of grids $G_k, G_{k-1}, \ldots, G_0$ is used, where G_k is the finest and G_0 the coarsest. A straightforward full approximation storage (FAS) multigrid scheme is applied to the system of equations. In the following notation the indices (i, j) are suppressed for convenience. Let $\widetilde{L}_k$ be the discrete approximation to the operator matrix $\widetilde{L}$ and $\mathbf{q}_k$ be the solution on the k-th grid. Also, let $\widetilde{L}_{k-1}$ be the coarse-grid operator, I_k^{k-1} be the fine-to-coarse grid restriction operator, and I_{k-1}^k be the coarse-to-fine grid prolongation operator. If $\hat{\mathbf{q}}_k$ is the current solution on grid k, the residual on this grid is $\mathbf{r}_k \equiv \mathbf{f}_k - \widetilde{L}_k \hat{\mathbf{q}}_k$. This leads to the coarse-grid equation

$$\widetilde{L}_{k-1}\mathbf{q}_{k-1} = \mathbf{f}_{k-1} = I_k^{k-1}\mathbf{r}_k + \widetilde{L}_{k-1}\left(I_k^{k-1}\hat{\mathbf{q}}_k\right). \tag{32}$$

After solving the coarse-grid equation for $\mathbf{q}_{k-1}$, the fine-grid solution is corrected by

$$\mathbf{q}_k \leftarrow \hat{\mathbf{q}}_k + I_{k-1}^k\left(\mathbf{q}_{k-1} - I_k^{k-1}\hat{\mathbf{q}}_k\right). \tag{33}$$

Equation (32) is solved by applying the same relaxation procedure that is used to solve the fine-grid equation. Multigrid is applied recursively to the coarse-grid equation. On the coarsest grid, many relaxation sweeps (typically 20 sweeps) are performed to ensure that the equation is solved completely.

The intergrid transfer operators are standard ones (e.g., see [7] or [5]). A full weighting restriction operator is used to transfer residuals. The transfer of the solution from a fine grid to a coarse grid is done with simple injection. Coarse-grid corrections are transferred with a bilinear interpolation operator, which is the adjoint of the restriction operator. A conventional W–cycle is used to execute the multigrid process.

6 SKIN FRICTION

For wall-bounded shear layers accurate prediction of surface skin friction is generally considered an essential requirement of an algorithm for computing viscous flows. In the case of Cartesian coordinates the skin friction is defined by

$$C_f = \frac{2\tau_w}{Re}, \quad \tau_w = u_y, \tag{34}$$

where the velocity component parallel to the surface u is nondimensionalized by the free-stream velocity and the coordinate normal to the surface y is scaled by the reference length for the Reynolds number Re. Thus, the surface shear stress τ_w is determined by the normal gradient of the velocity parallel to the solid surface. In the case of curvilinear coordinates (ξ, η) the wall shear stress can be computed from

$$\tau_w = \nabla V_t \cdot \mathbf{n}, \quad \mathbf{n} = \frac{\nabla \eta}{|\nabla \eta|}, \tag{35}$$

where V_t is the velcity component parallel to the surface and $\mathbf{n}$ is the unit normal to the surface. Assume that a constant η curve coincides with the solid surface. Also, let J be the Jacobian for the transformation $(x, y) \to (\xi, \eta)$. The inner product of Eq. (35) gives

$$\tau_w = \frac{(x_\xi^2 + y_\xi^2)^{1/2}}{J^{-1}} (V_t)_\eta, \tag{36}$$

and $J^{-1} = x_\xi y_\eta - x_\eta y_\xi$.

In cell-centered finite-volume schemes the wall shear stress is often computed with a two-point one-sided difference for V_t divided the normal distance from the first interior point to the wall. A Taylor series expansion shows that this approximation is second order only when the velocity profile is linear near the surface. With the present incompressible scheme, which uses finite-differencing for the advection terms, such an approximation was always first order. Even in the case of Hiemenz flow, which is planar stagnation flow without surface curvature, the behavior of this approximation was first order. In the numerical computation of τ_w the quantity $(V_t)_\eta$ is discretized with a second-order one-sided difference. The transformation derivatives x_η and y_η are also approximated with one-sided differences. The derivatives x_ξ and y_ξ are approximated with central differencing.

The skin-friction drag coefficient is determined by

$$(C_d)_f = \int_{\Gamma_{surf}} C_f ds, \tag{37}$$

where s is distance along the surface boundary Γ_{surf}. The trapezoidal rule is used for the numerical evaluation of the integral in Eq. (37). With the second-order approximation for $(V_t)_\eta$ the computed $(C_d)_f$ for Hiemenz and circular-arc stagnation flows, as well as parabola flow, was found to be second order with mesh refinement.

7 NUMERICAL RESULTS

The numerical scheme described in the previous sections was applied to three incompressible, viscous flow problems. As an initial evaluation of the scheme, high Reynolds number flow past a flat plate at zero incidence was considered. Then the effect of geometric curvature and Reynolds number on the behavior of the present scheme was examined by considering flow around a parabola
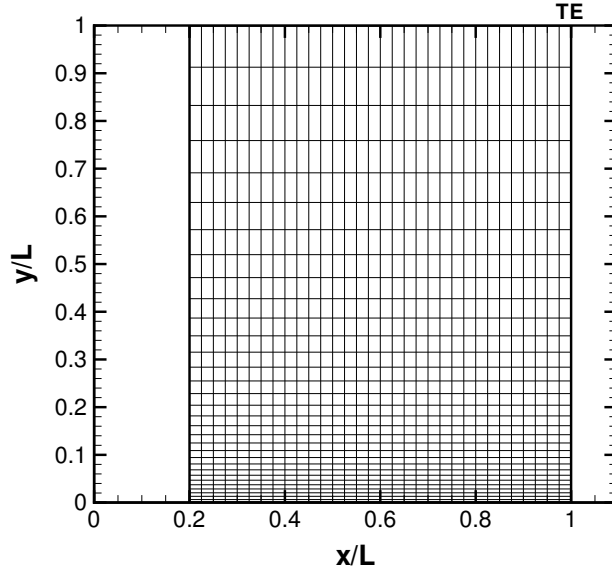
Figure 3: Domain of flat plate flow with 33×33 grid.

(representing an airfoil leading edge). For the final problem the scheme was applied to flow over a symmetric Kármán-Trefftz airfoil. Computational results are given for two different angles of attack.

7.1 Flat Plate

The computational domain for the flat plate simulation is displayed in Fig. 3. The plate begins at $x/L = 0$, the inflow boundary is at $x/L = 0.2$, and the outer boundary is at $x/L = 1$. The upper boundary is located one plate length away from the plate ($y/L = 1$). At the inflow boundary, the Blasius (self-similar) solution was prescribed. For the upper and downstream boundaries the pressure was set to the free-stream value p_∞, and the velocity components tangential to these outflow boundaries were defined according to the Blasius solution. The no-slip condition was imposed on the plate ($x/L = 0.2$ to $x/L = 1$).

The finest grid used for the flat plate calculations consisted of 512×512 cells. The grid spacing in the x direction was uniform. In order to resolve the boundary layer on the plate the grid was clustered at $y/L = 0$ and stretched geometrically to $y/L = 1$ (see Fig. 3). For this grid the minimum spacing in the y direction was 0.000375, and the stretching factor was 1.0053. A series of nested coarse grids was obtained by coarsening the fine grids by a factor of two in each coordinate direction. In all cases shown below, the coarsest grid was 16×16 cells.

Line Gauss-Seidel relaxation was used for the computations. The complete relaxation process involved one sweep with vertical line solves and one sweep with horizontal line solves, along with some additional work near the plate. The relatively small amount of additional work is needed due to the coupling of the flow equations near the plate. Moreover, the points for $j \leq 3$ were relaxed with 3-5 sweeps of horizontal solves. For the vertical line solves relaxation was initiated at the inflow boundary ($x/L = 0.2$) and proceeded to the outflow boundary ($x/L = 1$). With vertical solves underrelaxation was applied at 5-10 points near the plate. The underrelaxation

factor was $(1 + \beta)^{-1}$, where β was between 0.5 and 1.0. In the case of the horizontal line solves relaxation started at the outer boundary ($y/L = 1$) and continued to the inner boundary ($y/L = 0$). A $W(1, 1)$ multigrid cycle was used; that is, one complete relaxation process was performed on each grid before restricting to the coarse grid, and one complete relaxation process was performed after the coarse-grid correction was added to the fine-grid solution.

The Reynolds number of the flow past the flat plate was $10,000$. Figures 4 and 5 show the variation of the tangential velocity component u and the transverse velocity component v with the scaled normal coordinate η. Both velocity components are nondimensionalized by the boundary-layer edge velocity (u_e). The scaled v is multiplied by $Re_x^{1/2}$, where Re_x is the Reynolds number based on x, to obtain the self-similar solution, and the coordinate $\eta = 5y/\delta$, where δ is the thickness of the boundary layer. The computed velocity profiles are at the midplate location. Starting with the 32×32 cell grid, which has only seven points in the boundary layer, there is excellent agreement with the classical Blasius tangential velocity. There is good agreement with the Blasius transverse velocity with just seven points in the boundary layer.

In Figs. 6 and 7 the convergence behavior of the scheme for the flat plate flow is shown. The L_2 norm of the residuals for the pressure and momentum equations is given for each $W(1, 1)$ cycle in Fig. 6. In the full multigrid (FMG) process a single grid calculation was performed on the 17×17 grid. The multigrid algorithm was applied at each successive level of the FMG process. For most of the grids the residuals are reduced more than 6 orders of magnitude in 10 cycles. The convergence rates on the finest grid (513×513) for the three flow equations are 0.12 to 0.15. On the two finest grids the residuals are essentially reduced to machine zero. According to local mode analysis (Brandt[13]) the smoothing factor for relaxation with line solves is $5^{-1/2}$. Assuming only radial line solves in the W(1,1) cycle, the residual reduction per cycle would be 0.2. Due to the azimuthal line solves a faster convergence rate is attained.

Figure 7 shows the variation of the ratio of algebraic error to discretization error for the skin-friction drag coefficient of the plate. The skin-friction C_f is calculated from $x/L = 0$ to $x/L = 0.2$ by assuming it has an inverse square root behavior in distance from the leading edge of the plate (see Thomas, Diskin, and Brandt[9]). Numerical integration with the trapezoidal rule of C_f over the entire plate yields the drag coefficient. For all levels of grid refinement the algebraic error is reduced below the truncation error in a single multigrid cycle. Such performance of a scheme may be interpreted as an alternative definition of an optimally convergent scheme.

As indicated in Figs. 8 and 9, the solution on the finest grid can be obtained in a FMG process involving only one multigrid cycle on each grid considered in Fig. 6. The behavior of surface skin friction with mesh refinement is displayed in Fig. 10. In this figure N_y denotes the number of points in the y-direction. Also, the zero subscript refers to a mesh with 97 points in the normal direction and a stretching factor of 1.03 when the upper boundary of the domain is at $y_{max}/L = 1.0$. Calculated results are given for two different locations of the upper boundary. The linear variation of the skin-friction ratio $C_f/(C_f)_{Blasius}$ with the mesh spacing squared demonstrates second-order accuracy for the skin friction.
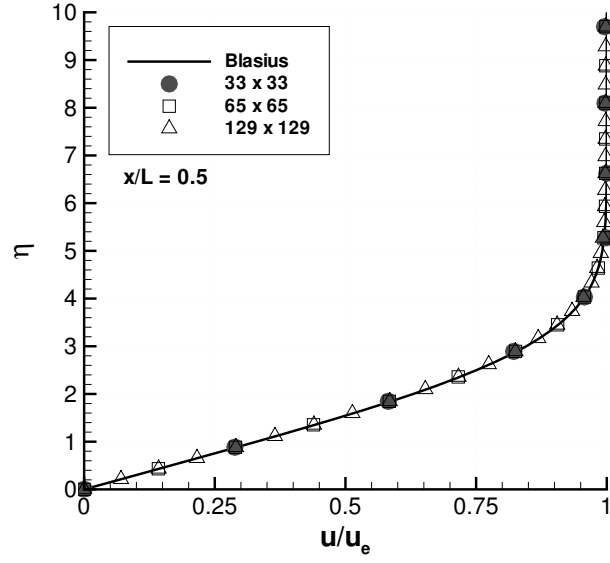
Figure 4: Tangential velocity profiles at midplate location for laminar flow over flat plate ($Re_L = 10,000$).

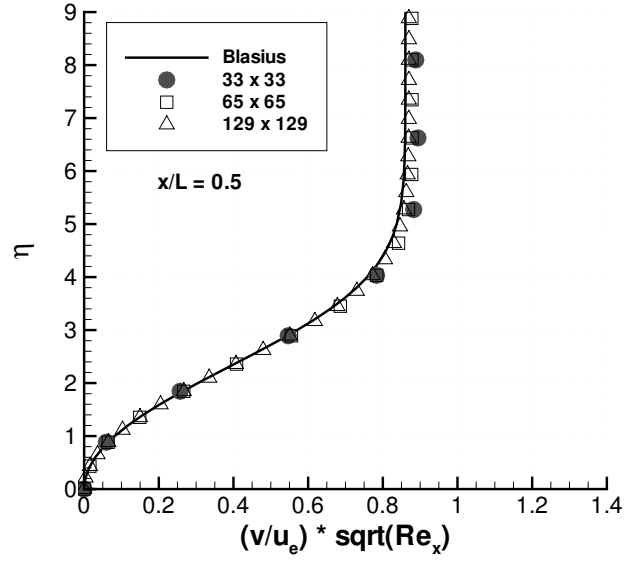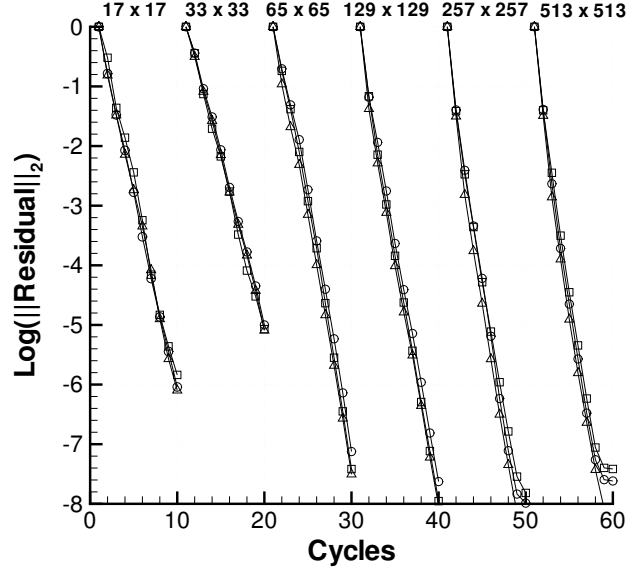Figure 5: Transverse velocity profiles at midplate location for laminar flow over flat plate ($Re_L = 10,000$).

Figure 6: Convergence behavior for laminar flow over flat plate ($Re_L = 10,000$). Residual symbols: Circle for pressure, square for x-momentum, triangle for y-momentum.
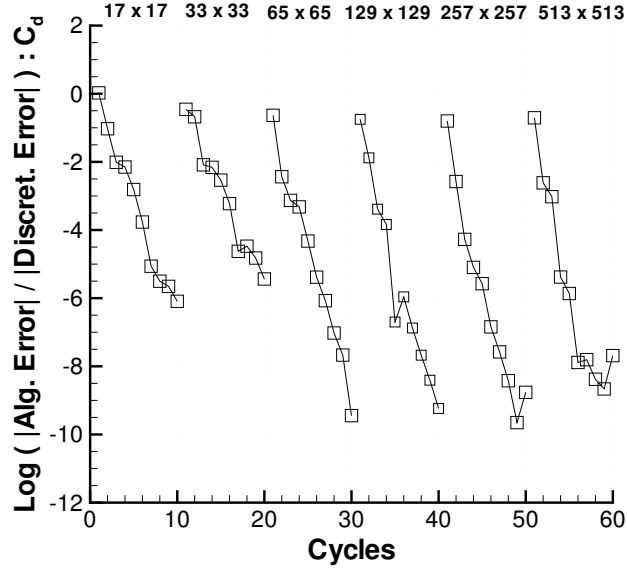

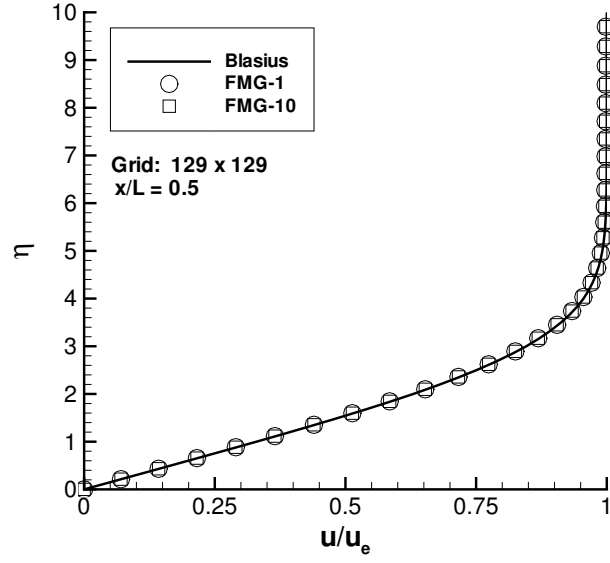Figure 7: Convergence behavior of drag coefficient for laminar flow over flat plate ($Re_L = 10,000$).

Figure 8: Variation with multigrid cycles of tangential velocity profile at midplate location for laminar flow over flat plate ($Re_L = 10,000$, 129×129 grid).
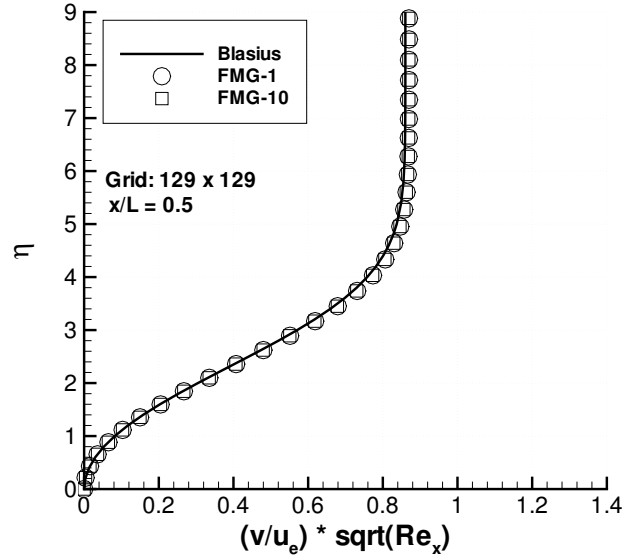
Figure 9: Variation with multigrid cycles of transverse velocity profile at midplate location for laminar flow over flat plate ($Re_L = 10,000$, 129×129 grid).

16
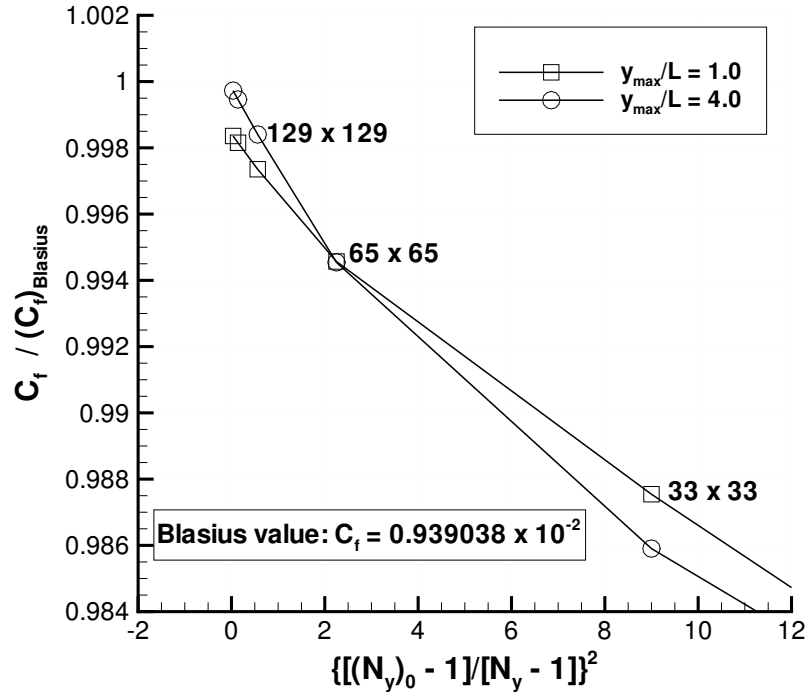
Figure 10: Behavior with mesh refinement of surface skin friction for laminar flow over flat plate ($Re_L = 10,000$).
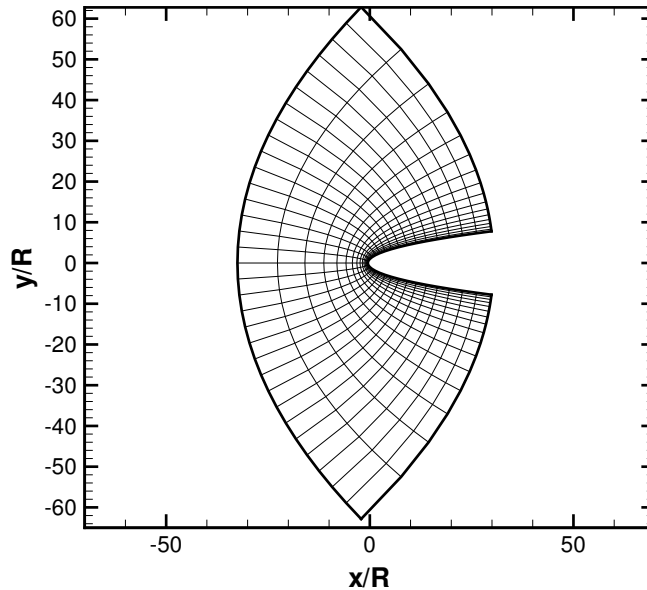
Figure 11: Coarse grid (33 x 17) for laminar flow over parabola.

7.2 Parabola

The flow over a parabola was determined with a conformal mapping. For the parabola, the leading edge radius of curvature R is the reference length. In the mapping a rectangular region in the complex z-plane was mapped to a region in a complex ζ-plane with inner (solid surface) and outer (inflow) boundaries defined by parabolas. The surface length of the inner boundary is 2, and the distance between the vertices of the inner and outer parabolas is 1. The physical problem in the z-plane is planar stagnation (Hiemenz) flow. In the computations the velocity at the outer boundary is specified according to the complex velocity in the ζ-plane. At the outflow boundary the pressure and the velocity tangent to the boundary are specified, resulting in a well-posed problem for the full Navier-Stokes equations. The pressure is the free-stream value, and the tangential velocity is obtained from the complex velocity in the ζ-plane.

Laminar flow over the parabola at three different Reynolds numbers was considered. The Reynolds numbers based on radius of curvature were $Re_R = 25$, $Re_R = 100$, and $Re_R = 312.5$, which correspond to Reynolds numbers based on unit airfoil chord of $Re_c = 800$, $Re_c = 3200$, and $Re_c = 10000$, respectively. In Fig. 11 a coarse grid for the calculations is shown. Figure 12 presents the variation in the error of the continuity equation with mesh refinement. Second-order accuracy of the scheme is essentially realized on the 129×65 grid for all Reynolds numbers. In Fig. 13 the change in surface skin-friction error, at the location midway between the vertex of the parabola and the upper outflow boundary, with mesh density is shown. Second-order accuracy begins on the 65×33 grid. Numerical experiments indicate that the principal parameter affecting the onset of second-order behavior is the curvature at the leading edge of the parabola. Moreover, as the radius of curvature is increased, the mesh density for the onset of design accuracy decreases.

In Table 1 second-order accuracy is also demonstrated for the drag coefficient (C_d) of the parabola at each Re_R. The value of the C_d is given for both one multigrid cycle (FMG-1) and ten
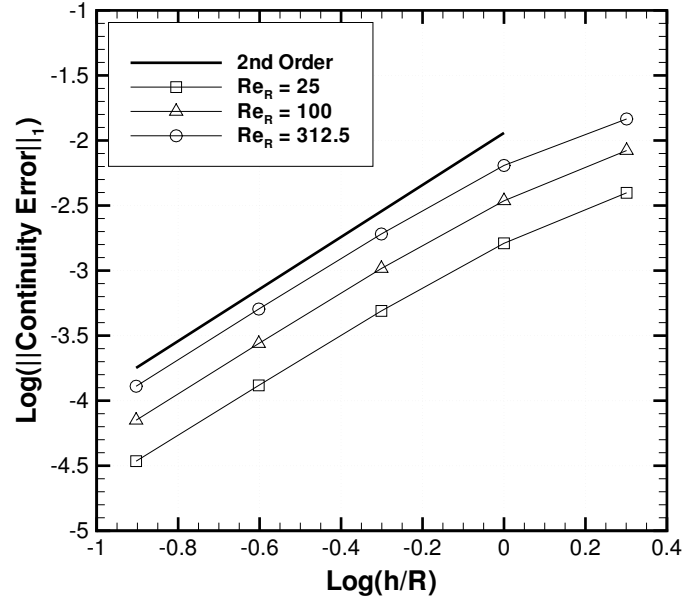
18

Figure 12: Behavior of continuity with mesh refinement and Reynolds number for laminar flow over parabola. Mesh range: $17 \times 9 \rightarrow 513 \times 257$.
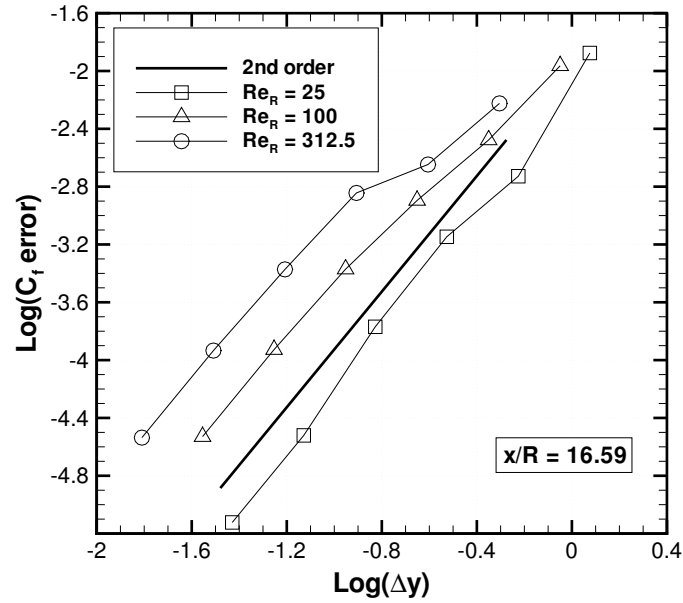

Figure 13: Variation of skin friction error with mesh refinement and Reynolds number for laminar flow over parabola. Mesh range: $17 \times 9 \rightarrow 513 \times 257$, Axial location: $x/R = 16.59$.

Re_R	$N_x \times N_y$	C_d (FMG-1)	C_d (FMG-10)	$|e_a|/|e_d| : C_d$ (FMG-1)
25	17×9	1.070609	1.030401	0.029153
	33×17	1.489693	1.535983	0.283019
	65×33	1.603028	1.617511	0.288438
	129×65	1.641015	1.643881	0.234462
	257×129	1.649742	1.651158	0.404654
	513×257	1.649895	1.652720	0.844388
100	17×9	0.466985	0.445406	0.041222
	33×17	0.552725	0.677579	0.512038
	65×33	0.725510	0.758993	0.469649
	129×65	0.783574	0.787396	0.288910
	257×129	0.794248	0.794577	0.128796
	513×257	0.795718	0.796246	0.487271
312.5	17×9	0.224233	0.208086	0.059588
	33×17	0.230412	0.344023	0.534571
	65×33	0.363082	0.397327	0.427955
	129×65	0.423235	0.431337	0.407791
	257×129	0.440050	0.440120	0.022917
	513×257	0.441890	0.442357	0.384757

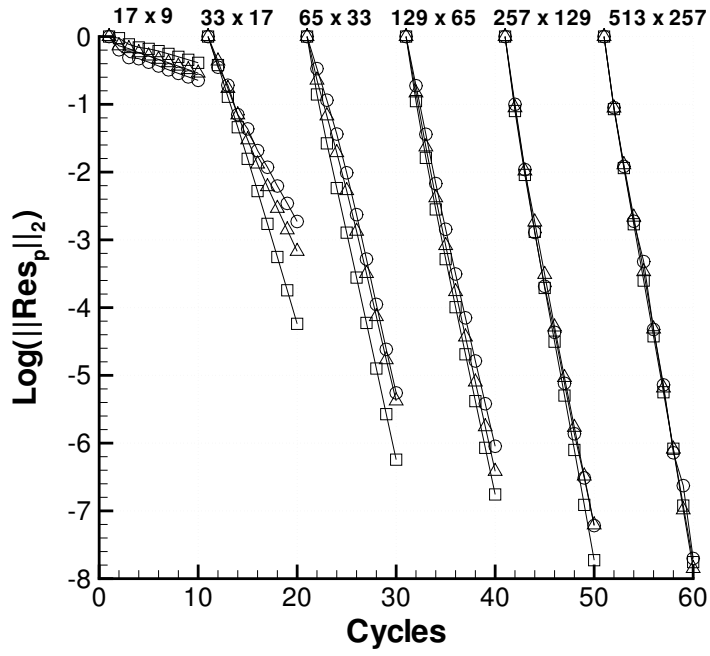Table 1: Drag coefficient at different Reynolds numbers for laminar flow over parabola.

Figure 14: Effect of Reynolds number on solution convergence for laminar flow over parabola. Residual symbols: circle for $Re_R = 25$, square for $Re_R = 100$, triangle for $Re_R = 312.5$.

cycles (FMG-10). In addition, the ratio of the algebraic error to the discretization error, $|e_a|/|e_d|$, is presented for each grid. The algebraic error is reduced below the truncation error in one cycle for all grids and all Reynolds numbers. Thus, for this flow over a body with curvature, the present scheme satisfies the alternative definition of an optimally convergent scheme.

In Fig. 14 the effect of Reynolds number on the convergence behavior for the parabola flow is shown. The residual is for the pressure equation. Convergence behavior is similar for the higher mesh densities (i.e., 129×65 and greater) at each Reynolds number, and rapid convergence with at least a rate of 0.2 per cycle is attained for these mesh sizes. As the mesh density decreases (i.e., 65×33 and smaller), the convergence rate becomes slower and the influence of Reynolds number on the rate becomes greater. Such coarse grid slowdown has been observed for inviscid flows (Roberts and Swanson [11]) as well as viscous flows being considered here. One possible explanation for this behavior is the larger discretization error on coarser grids associated with the relaxation process. Thus, whenever the resolution on the coarser grids in the FMG procedure is not adequate, one would anticipate convergence slowdown.

7.3   Airfoil

Solutions were obtained for incompressible, viscous flow around a symmetric Kármán-Trefftz airfoil at zero and two degrees angle of attack. The Reynolds number based on chord (Re_c) was varied from 200 to 800. A Kármán-Trefftz airfoil was generated from a cylinder by a conformal mapping [19]. The trailing-edge angle is $10°$, and the thickness ratio is approximately 15 percent. The airfoil flow was solved on a finite domain. At inflow points along the outer boundary the free-stream velocity components were specified. For outflow points the free-stream pressure was prescribed, and the streamwise diffusion for the tangential momentum equation was taken to be zero.

The present scheme is compared with Runge-Kutta (R-K) and implicit upwind based multigrid schemes. These other two schemes solve the compressible Navier-Stokes equations, and they do not include preconditioning. Thus, as the Mach number goes to zero, these schemes can experience inaccurate discretization and slow convergence, or even divergence. In order to have representative convergence of the schemes, and at the same time have the Mach number sufficiently low for comparison purposes, the free-stream Mach number (M_∞) for the calculations with the R-K and implicit upwind schemes was taken to be 0.1. The downstream outflow boundary pressure p_e was specified in the calculations with the compressible flow solvers. Thus, to simulate the incompressible flow and be able to compare with the solution from the incompressible flow solver, it was necessary to increment the pressure p_e. For example, with the outer boundary at three chords, the modified pressure $p_e^* = p_e + \Delta p = 1.00015$ when $M_\infty = 0.1$, and $\Delta p = 0.00015$. As $M_\infty \to 0$, then $\Delta p \to 0$.

To facilitate the resolution of the near and far wake regions, especially in the case of laminar flow where the mixing rate due to the physical diffusion is slow, a C-type mesh was generated for the airfoil calculations. A hyperbolic grid generator was used to create the mesh. The near field part of the grid is depicted in Fig. 15. The outer boundary of the domain is roughly 3 chords from the airfoil. The coarsest grid in the grid sequence for the multigrid solver contained 16×8 cells. On each grid a relaxation sweep started at the radial line emanating from the airfoil leading edge, proceeded over the upper half of the domain, and then over the lower half of the domain. The relaxation sweep with radial solves was followed by a relaxation sweep with azimuthal solves that started at the outer C-type boundary. Then, 3-5 additional sweeps with azimuthal solves were performed near the solid surface boundary ($j \leq 3$). This is done to reduce the residuals near the boundary so that they are comparable in size to residuals in the interior.

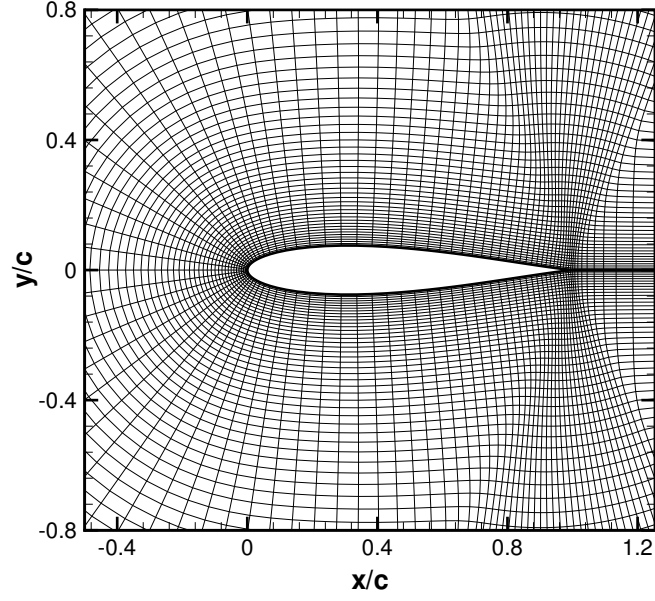In Fig. 16 the convergence histories for this nonlifting case are presented. The average rate

Figure 15: Near field of 128 x 64 cell C-type grid for computing laminar flow over Kármán-Trefftz airfoil ($Re_c = 200$).
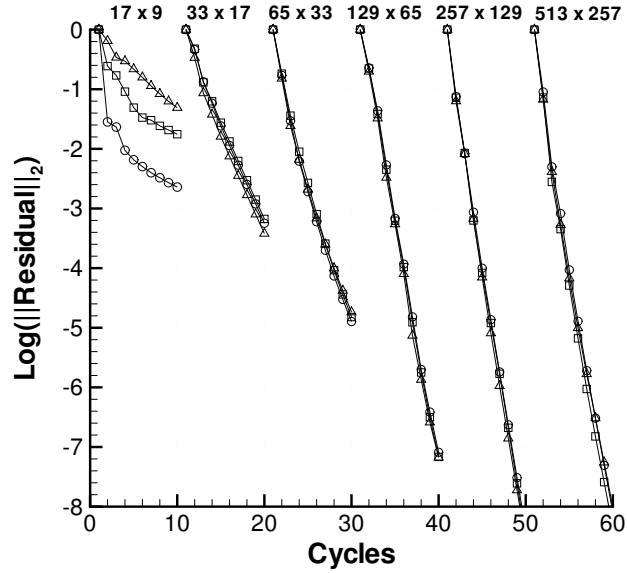

Figure 16: Convergence behavior for laminar flow over nonlifting Kármán-Trefftz airfoil ($\alpha = 0°$, $Re_c = 200$). Residual symbols: Circle for pressure, square for x-momentum, triangle for y-momentum.

Scheme	MG Cycle	WU/cycle	Tridiag Solves/ $N_x N_y$	N_{cycle} $\|Res\|_2 \leq 10^{-4}$
INCOMP	W(1,1)	10.7	20	5
5 stage R-K	W(1,0)	12	36	124
Implicit upwind	W(1,0)	4	12	485

Table 2: Computational work for incompressible, 5-stage R-K, and implicit upwind schemes.

of reduction of the residual on the 513×257 grid is about 0.11 for the pressure and momentum equations. There is again somewhat slower convergence on the coarser meshes, with about five orders of magnitude reduction of the residuals on the 65×33 grid.

In order to estimate the relative work required by the present, R-K, and implicit upwind schemes, we consider an operation count based on residual evaluations, tridiagonal solves, and the number of cycles to achieve a specific reduction in residuals. First we define the work associated with residual evaluations. For a W(m, n) multigrid cycle, there are $m + n + 1$ residual evaluations per cycle on the fine grid. Let WU represent work units. A work unit is often defined to be one relaxation sweep of the finest grid. Thus, a WU can be considered as the cost of a vector residual evaluation on the finest grid. In this assessment we neglect the cost of interpolating the residuals and solutions between the grid levels. For a W(m, n) cycle, we have that

$$
\begin{aligned}
\frac{\text{WU}}{W\text{–cycle}} &\approx [k(m + n) + 1](1 + \frac{1}{2} + \frac{1}{4} + \cdots) \\
&= 2[k(m + n) + 1],
\end{aligned} \tag{38}
$$

where k denotes the number of sweeps on each grid that require a vector residual evaluation. If line solves are considered in each coordinate direction, then $k = 2$. In the case of a five stage R-K scheme, $k = 5$. The WU per cycle for the current scheme with a W(1,1) cycle that includes one radial relaxation sweep and one azimuthal relaxation sweep (neglecting additional work at surface boundary with azimuthal solves) is 10.

When a finite-volume formulation is used for the discretization of the flow equations and alternating line Gauss-Seidel relaxation is applied as in the scheme of Swanson [12], an additional residual evaluation is incurred due to the Gauss-Seidel updating of the solution. Since a finite-difference discretization is used for the momentum equations in the present scheme, there is only a 1/3 additional vector residual calculation (due to the pressure equation) for each relaxation sweep. If we include that in the operation count, the WU per cycle for the present scheme would be increased to approximately 10.7. Both the R-K and implicit upwind schemes apply a W(1,0) cycle, and the WU per cycle for these schemes is given in Table 2.

For the three schemes there is a difference in computational effort resulting from scalar tridiagonal and pentadiagonal inversions. As indicated previously each relaxation sweep of the present scheme requires one tridiagonal solve and two pentadiagonal solves (corresponding to the three flow equations) for the grid lines not in the direction of the relaxation. Since the operation count for a pentadiagonal inversion is about two times that for a tridiagonal inversion, the work required on the fine grid with $m + n = 2$ and $k = 2$ is roughly proportional to that for 20 tridiagonal solves. Since the present scheme is solving three equations, we assume, for an equitable comparison of operation count, that all schemes are solving three equations. For the R-K scheme there is a scalar

Scheme	$W_{res}/(N_{ops})_{res}$	$W_{tri}/(N_{ops})_{tri}$	$Work$
INCOMP	54	200	8296
5 stage R-K	1488	8928	255936
Implicit upwind	1940	11640	333680

Table 3: Comparison of work required by three Navier-Stokes schemes (grid: 513×257).

tridiagonal inversion for each flow equation, each coordinate direction, and each of the five stages due to the residual smoothing procedure used to extend stability. In addition, there is similar work performed on the prolongated coarse grid corrections. Thus, the work due to this part of the scheme is proportional to 36 tridiagonal solves. Thus, the R-K scheme considered here [20] requires almost two times as many tridiagonal inversions as the present scheme. It should also be pointed out that the R-K scheme used here is a (5,3) scheme, which means that the complete residual, including viscous and numerical dissipation terms, is evaluated only on three stages. This factor has not been taken into account. With the implicit upwind scheme there are six scalar tridiagonal inversions because a diagonalized version of the scheme is used. In the diagonalization procedure there are three matrix-vector multiplies, and for a system of three equations, these correspond to roughly six tridiagonal solves. Thus, the implicit upwind scheme requires about 12 scalar tridiagonal solves.

We now sum the work contributions due to residual evaluations and tridiagonal solves. Let W_{res} and W_{tri} denote the work associated with residual evaluations and tridiagonal solves, respectively. Then, the total work per grid point required by a scheme can be approximated by

$$Work = W_{res} + W_{tri} \tag{39}$$

where

$$W_{res} = (\text{WU/cycle}) \, (N_{ops})_{res} \, N_{cycles}, \tag{40}$$
$$W_{tri} = 2 \, N_{tri} \, (N_{ops})_{tri} \, N_{cycles}, \tag{41}$$

with N_{ops} representing the number of operations needed to evaluate the residual vector function, N_{tri} being the number of tridiagonal solves per total number of points $(N_x N_y)$, $(N_{ops})_{tri}$ denoting the number of operations in a scalar tridiagonal solve (3 adds, 3 multiplies, and 2 divides for a total of 8 operations), and N_{cycles} being the number of cycles needed to reduce the residuals a predetermined number of decades. The factor of two in Eq. (41) is due to the multigrid process. According to [22] the residual (based on central differencing with numerical dissipation) of the diagonalized implicit algorithm requires 124 operations (i.e., 48 adds, 72 multiplies, 4 divides). Then, an estimate for the ratio of $(N_{ops})_{res}$ to $(N_{ops})_{tri}$ is 16. If we assume that $(N_{ops})_{res}$ is about the same for all schemes, the contributions of both W_{res} and W_{tri} to the $Work$ (see Table 3) indicate that the present scheme is more than 30 times faster than the other schemes for the finest mesh (i.e., 513×257). For a mesh density of 129×65 the speedup of the present scheme exceeds an order of magnitude. This improvement in the computational effort relative to the R-K and implicit upwind schemes is also evident in the variation of the drag coefficient (C_d) with multigrid cycles (see [12]).

The total drag coefficient (C_d), along with the pressure and skin-friction contributions $((C_d)_p$ and $(C_d)_f$, respectively) computed with the three schemes on the 513×257 grid are given in Table 4. The maximum variation in C_d divided by the INCOMP scheme value is 2.2 percent. There is an

Scheme	$(C_d)_p$	$(C_d)_f$	C_d
INCOMP	0.074780	0.222239	0.297019
5 stage R-K	0.076662	0.226987	0.303649
Implicit upwind	0.071351	0.227320	0.298670

Table 4: Drag coefficients for laminar flow over Kármán-Trefftz airfoil computed with three different schemes ($\alpha = 0^o$, $Re_c = 200$, grid: 513×257).

unexpected difference between the $(C_d)_p$ for the implicit upwind scheme and the other schemes. The error behavior of the drag coefficients with mesh refinement was determined. For all algorithms the variation in $(C_d)_p$ error (based on a Richardson extrapolated value) with mesh refinement is at least second order. The error in $(C_d)_f$ obtained with the R-K and implicit upwind schemes does not decrease in a monotonic manner with reduction in mesh spacing. Although there is a monotonic decrease in $(C_d)_f$ error for the INCOMP scheme, the error is only first order. Thus, none of the algorithms exhibit second-order accuracy for the total drag error.

In Figs. 17-22 the pressure and skin-friction distributions computed with the present scheme on various grid densities are compared with the fine grid results obtained with the R-K scheme (where the free-stream Mach number was set to 0.1). There is generally very good agreement starting with the 129×65 grid for both the nonlifting and lifting flows. Figures 23 and 24 show the variation in the error of pressure and skin-friction near the location of peak skin friction. The error of each quantity is determined from the corresponding Richardson extrapolation value. Both the pressure and skin friction exhibit, in this region of strong flow gradients, essentially second-order behavior.

The behavior of solution error with respect to mesh refinement is displayed in Fig. 25 and Fig. 26. The solution on the 513×257 grid is used to determine the error. Figure 25 shows that the L_2 norms of the errors, excluding boundary points, in the solution variables u, v, and p exhibit second-order accuracy. In addition, this figure reveals that the error in the continuity equation decreases in a first-order manner. The derivatives in the continuity equation are approximated with central differencing. Error variations in the flow quantities along the wake line ($x/c > 1$, $y/c = 0$) are presented in Fig. 26. The pressure error diminishes with second-order accuracy. As the streamwise grid stretching factor (equal to 1.075 on the finest mesh) in the wake decreases with mesh refinement, the error in the velocity component u is approaching second-order behavior. In the case of the continuity equation, the error appears to be going to a constant as the mesh is refined. A mass conservation error is generated at the airfoil trailing edge, and this error is being transported by advection and diffusion as the flow proceeds downstream. The occurrence of such an error certainly indicates that an improvement is required in the accuracy of the discretization of the pressure equation (i.e., boundary condition) at the trailing edge. At the same time, it should be emphasized that the solution on the airfoil does not appear to be significantly compromised, as comparisons with solutions computed with other methods have demonstrated.

Pressure and velocity contours for the lifting solution on the 513×257 C-type grid are depicted in Figs. 27 and 28. The thickness of the attached boundary layer is about 0.25 airfoil chord, and there are about 70 points in the boundary layer at the midchord location. Slow diffusion of the airfoil wake is evident.

As indicated previously the outer boundary (OB) for the initial set of calculations was located only about 3 chords (approximately 12 boundary-layer thicknesses) away from the surface of the

Re_c	$(C_d)_p$	$(C_d)_f$	C_d
200	0.070366	0.211714	0.282080
400	0.056302	0.141830	0.198132
600	0.049628	0.112108	0.161736
800	0.045483	0.094836	0.140319

Table 5: Variation of drag coefficient with Reynolds number for laminar flow over airfoil (Kármán-Trefftz, $\alpha = 0^o$, grid: 641×449).

Re_c	$(C_d)_p$	$(C_d)_f$	C_d
200	0.070210	0.211399	0.281609
400	0.056185	0.141690	0.197875
600	0.049527	0.112031	0.161558
800	0.045390	0.094794	0.140184

Table 6: Variation of drag coefficient with Reynolds number for laminar flow over airfoil (Kármán-Trefftz, $\alpha = 0^o$, grid: 897×513).

airfoil. Thus, a series of nonlifting computations were performed to assess the influence of the OB location on the solutions. The OB location was varied between 3 chords and 20 chords. For each different location of the boundary the same grid stretching factor was maintained in the directions normal to the airfoil surface and downstream of the airfoil trailing edge. The effect of the OB distance, which is designated by R, on the skin-friction and total drag coefficients is displayed in Fig. 29. The error in the two drag coefficients is based on values determined from Richardson extrapolation. There is only a 1.6 percent error in total drag when the OB is located at three chords.

The performance of the present scheme for the airfoil flow is now considered for different Reynolds numbers (Re_c). In Table 5 the variation of the pressure, skin-friction, and total drag coefficients with Re_c are given. These nonlifting solutions were computed with a mesh density of 641×449 and an OB location of 20 chords. This set of calculations was repeated with the tangential mesh spacing on the airfoil decreased by a factor of two and a reduction in the normal mesh spacing, resulting in a mesh density of 897×513. The drag coefficients for these computations are presented in Table 6. Differences between these two sets of results appear in the fourth decimal place. In Fig. 30 the convergence behavior on the 641×449 grid for $Re_c = 200$ is shown. The rates of convergence on the sequence of grids are essentially the same as those obtained for the sequence associated with the 513×257 grid having the OB at the 3 chord location. Convergence histories for $Re_c = 600$ and mesh densities of 641×449 and 897×513 are displayed in Figs. 31 and 32. The convergence rates on both mesh sequences are similar. On the 641×449 grid the convergence rate (average residual reduction rate) is about 0.13 per cycle. For the 897×513 grid the convergence rate is slightly slower (0.15 per cycle).

Figure 33 shows the logarithmic variation of the ratio of algebraic error to discretization error for the skin-friction drag coefficient of the airfoil. The present scheme nearly exhibits optimal

Re_c	C_l	$(C_d)_p$	$(C_d)_f$	C_d
200	0.089128	0.072462	0.210588	0.283050
400	0.084476	0.058133	0.140861	0.198994
600	0.079284	0.051275	0.111242	0.162517

Table 7: Variation of drag coefficient with Reynolds number for laminar flow over lifting airfoil (Kármán-Trefftz, $\alpha = 2^o$, grid: 641×449).

multigrid behavior, according to the alternative definition given previously. Only on the finest grid is the algebraic error not driven below the truncation error of the scheme in one multigrid cycle.

Solutions for the lifting Kármán-Trefftz airfoil were also obtained on the 641×449 grid with the OB at 20 chords. Computed drag coefficients corresponding to Re_c values of 200, 400, and 600 are given in Table 7. Convergence difficulties were encountered at $Re_c = 800$. A subsequent calculation done with the R-K scheme indicated flow separation on the airfoil upper surface near the trailing edge at this Reynolds number. The issues related to separated flows have not been considered in this report. Some of these issues, such as poor coarse-grid approximation, have been addressed by Brandt and Yavneh [8]. In addition, fast convergence has been obtained for the driven cavity problem, provided the Reynolds number of the flow is sufficiently low (i.e., $Re \leq 1000$). However, further effort is required to realize a second-order accurate scheme with optimal convergence when solving steady flow problems over a large Re range that have streamwise recirculation regions.

An effort to consider the effect on convergence rate of refinement in normal airfoil surface grid spacing and grid stretching was made. Reduction in the normal spacing required an increase in the magnitude of the underrelaxation parameter β, which is used near the airfoil surface when relaxing with radial lines. A doubling of the standard value was necessary to achieve stability and convergence. This increase in β introduced an unsatisfactory mesh sensitivity with respect to convergence. In addition, larger β values result in slower convergence. A possible remedy for this difficulty is to solve the flow equations fully coupled near the surface. Then there will be no requirement for an underrelaxation factor, and the robustness of the scheme should be significantly enhanced.

8 CONCLUDING REMARKS

A multigrid algorithm with essentially $O(N)$ behavior has been developed for the steady, incompressible Navier-Stokes equations. The momentum and pressure equations have been discretized with conventional finite-difference and finite-volume methods, respectively. A discrete approximation to the normal component of the momentum equation has been used as a vehicle for applying the divergence-free boundary condition for the pressure equation. Solutions have been obtained for laminar flow past a flat plate with essentially textbook multigrid efficiency. Furthermore, the multigrid method has been used to solve viscous flows with curvature effects. These geometries include a parabola and a Kármán-Trefftz airfoil. Fast convergence has been obtained for each of these flows. With the present scheme more than an order of magnitude reduction in computational effort has been achieved when compared with R-K and implicit upwind based multigrid schemes.

Solutions have been calculated for both nonlifting and lifting airfoil flows with Reynolds number (Re_c) varying between 200 and 800. Tables for aerodynamic coefficients have been presented.

For the lifting case with $Re_c = 800$ separation occurred and convergence was not possible. The capability to compute separated flows was outside the scope of this report.

It has been demonstrated that the dependent variables of the airfoil calculations exhibit a global second-order accuracy. Furthermore, it has been shown that the dependent variables have an order property in the wake region. However, these computations also indicate that an error is created in mass conservation at the airfoil trailing edge that is convected and diffused downstream. This error compromises the order property of the continuity equation in the wake region. Although there appears to be no significant effect on the solution in the vicinity of the airfoil, such behavior in the continuity equation certainly is not considered acceptable. Preliminary numerical results indicate that a stronger enforcement of continuity near the trailing edge can provide the necessary remedy.

The underrelaxation factor (β), which is used in conjunction with radial line solves at grid points near a solid surface boundary, can cause a slowdown in convergence. Such behavior has occurred when the normal mesh spacing at the surface becomes sufficiently small that the coupling of the flow equations requires a significant increase (i.e., a factor of two) in the standard β to maintain stability. This difficulty can be removed by solving the flow equations fully coupled near the surface. Then there would be no requirement for underrelaxation.

While fast convergence has been obtained on fine grids, the convergence on relatively coarse meshes in the FMG process has been somewhat slow. The sources of slower convergence rates on coarse grids need to be completely identified. One possible factor that can affect these convergence rates is the validity of the principal linearization on the coarse grids. That is, terms considered subprincipal for the relaxation process may have become principal. Another possible factor affecting these rates is the accuracy of the numerical boundary conditions as well as the choice of boundary conditions.

Further studies of the present scheme are also required to clearly delineate the effects of mesh aspect ratio and grid stretching on convergence rate, and thus, on the discrete factorizability of the algorithm. While significant gains in computational efficiency have been achieved for laminar flow, much greater gains (i.e., two orders of magnitude) are anticipated with the extension of factorizable schemes to allow computation of turbulent flows.

One viewpoint of the present scheme is that it represents a building block in a general class of algorithms for solving complex flows. For separated and turbulent flows the INCOMP scheme will have to perform in concert with other building blocks in order to attain optimal multigrid efficiency.

Acknowledgments

References

[1] Jameson, A., "Solution of the Euler Equations for Two Dimensional Transonic Flow by a Multigrid Method," *Appl. Math. Comput.*, vol. 13, nos. 3 and 4, pp. 327–355, 1983.

[2] Mulder, W., "Multigrid Relaxation for the Euler Equations," *J. Comput. Phys.*, vol. 60, no. 2, pp. 235–252, 1985.

[3] Anderson, W. K., Thomas, J. L., and Whitfield, D. L., "Three-Dimensional Multigrid Algorithms for the Flux-Split Euler Equations," NASA Technical Paper 2829, 1988.

[4] Warren, G. P., and Roberts, T. W., "Multigrid Properties of Upwind-Biased Data Reconstructions," *Sixth Copper Mountain Conference on Multigrid Methods,* NASA Conference Publication 3224, Part 2, 1993.

[5] Trottenberg, U., Oosterlee, C. W., Schüller, A., "Multigrid," Academic Press, 2001.

[6] Hackbush, W., "Multi-grid Methods and Applications," Springer-Verlag, 1985.

[7] Brandt, A., "Multigrid Techniques: 1984 Guide with Applications to Fluid Dynamics," GMD-Studie 85, GMD-FIT, 1985.

[8] Brandt, A., and Yavneh, I., "Accelerated Multigrid Convergence and High-Reynolds Recirculating Flows," *SIAM J. Sci. Stat. Comput.*, vol. 14, no. 3, pp. 607–626, 1993.

[9] Thomas, J. L., Diskin, B., and Brandt, A., "Distributed Relaxation Multigrid and Defect Correction Applied to the Compressible Navier-Stokes Equations," *AIAA Paper* 99–3334, 14th Computational Fluid Dynamics Conference, Norfolk, VA, July 1999.

[10] Sidilkover, D., and Ascher, U. M., "A Multigrid Solver for the Steady State Navier-Stokes Equations using the Pressure-Poisson Formulation," *Comp. Appl. Math.* vol. 14, no. 1, pp. 21–35, 1995.

[11] Roberts, T. W., and Swanson, R. C., "Extending Ideal Converging Multigrid Methods to Airfoil Flows," *AIAA Paper* 99-3337, 1999.

[12] Swanson, R. C., "Towards Optimal Multigrid Efficiency for the Navier-Stokes Equations," *AIAA Paper* 2001-2574, 2001.

[13] Brandt, A., "Mult-Level Adaptive Solutions to Boundary-Value Problems," *Math. Comp.*, vol. 31, no. 138, pp. 333–390, 1977.

[14] Gresho, P. M., and Sani, R. L., "On Pressure Boundary Conditions for the Incompressible Navier-Stokes Equations," *Int. J. Numer. Methods Fluids*, vol. 7, pp. 1111–1145, 1987.

[15] Henshaw, W. D., "A Fourth-Order Accurate Method for the Incompressible Navier-Stokes Equations on Overlapping Grids," *J. Comput. Phys.*, vol. 113, pp. 13–25, 1994.

[16] Henshaw, W. D., Kreiss, H.-O., Reyna, L. G. M. "A Fourth-Order Accurate Difference Approximation for the Incompressible Navier-Stokes Equations," *Computers and Fluids*, vol. 23, no. 4, pp. 575–593, 1994.

[17] Strikwerda, J., "Finite Difference Methods for the Stokes and Navier-Stokes Equations," *SIAM J. Sci. Stat. Comput.*, vol. 5, pp. 56–68, 1984.

[18] Petersson, N. A., "Stability of Pressure Boundary Conditions for Stokes and Navier-Stokes Equations," *J. Comput. Phys.*, vol. 172, pp. 40–70, 2001.

[19] Roberts, T. W., Sidilkover, D., and Swanson, R. C., "Textbook Multigrid Efficiency for the Steady Euler Equations," *AIAA Paper* 97-1949, 1997.

[20] Swanson, R. C. and Turkel, E., "Multistage Schemes with Multigrid for Euler and Navier-Stokes Equations - Components and Analysis," *NASA TP* 3631, August 1997.

[21] Krist, S. L., Biedron R. T. and Rumsey, C. L., "CFL3D User's Manual," *NASA TM* 1998-208444, 1998.

[22] Pulliam, T. H. and Chaussee, D. S., "A Diagonal Form of an Implicit Approximate-Factorization Algorithm," *J. Comput. Phys.*, vol. 39, pp. 347–363, 1981.
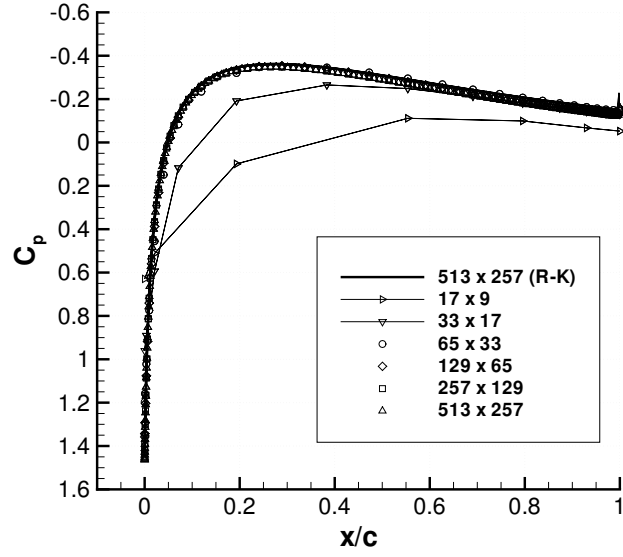
Figure 17: Surface pressure distribution for laminar flow over nonlifting Kármán-Trefftz airfoil ($\alpha = 0°$, $Re_c = 200$).
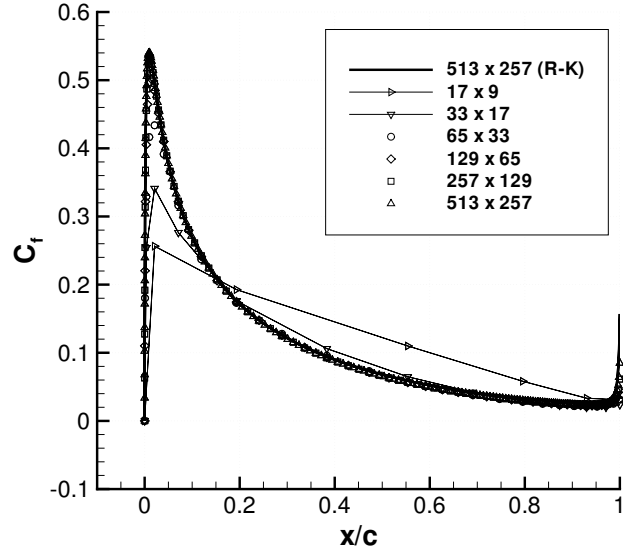
Figure 18: Surface skin-friction distribution for laminar flow over nonlifting Kármán-Trefftz airfoil ($\alpha = 0°$, $Re_c = 200$).
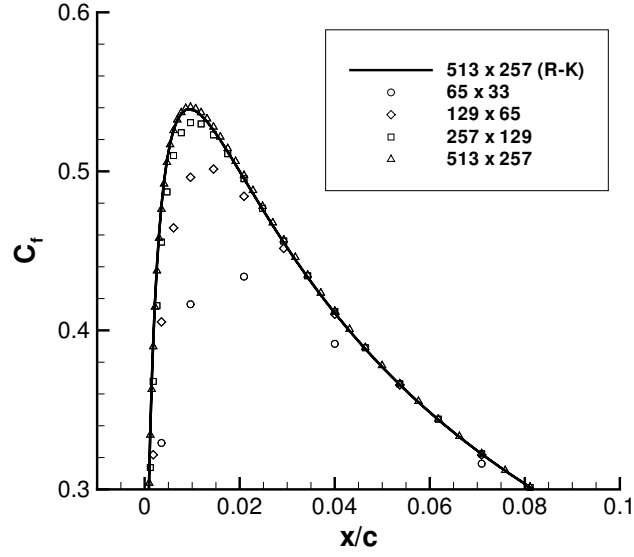
Figure 19: Blowup of Surface skin-friction distribution for laminar over nonlifting Kármán-Trefftz airfoil ($\alpha = 0°$, $Re_c = 200$).
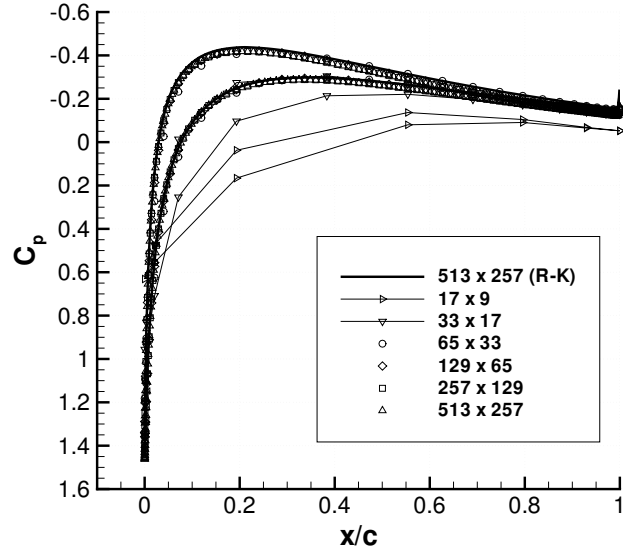
Figure 20: Surface pressure distribution for laminar flow over lifting Kármán-Trefftz airfoil ($\alpha = 2°$, $Re_c = 200$).
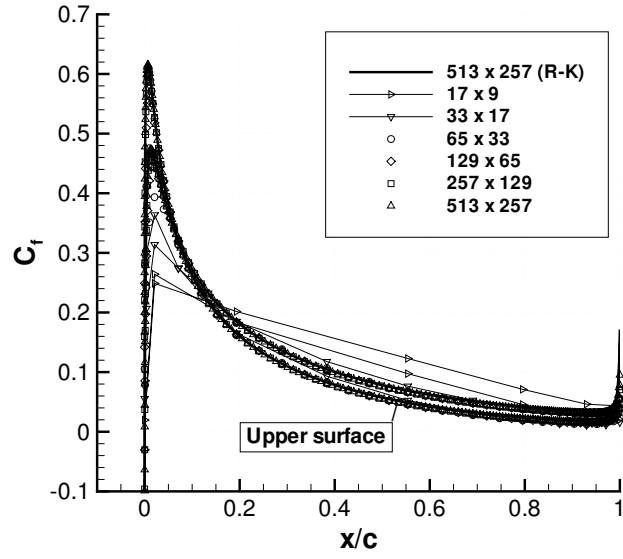
Figure 21: Surface skin-friction distribution for laminar flow over lifting Kármán-Trefftz airfoil ($\alpha = 2°$, $Re_c = 200$).
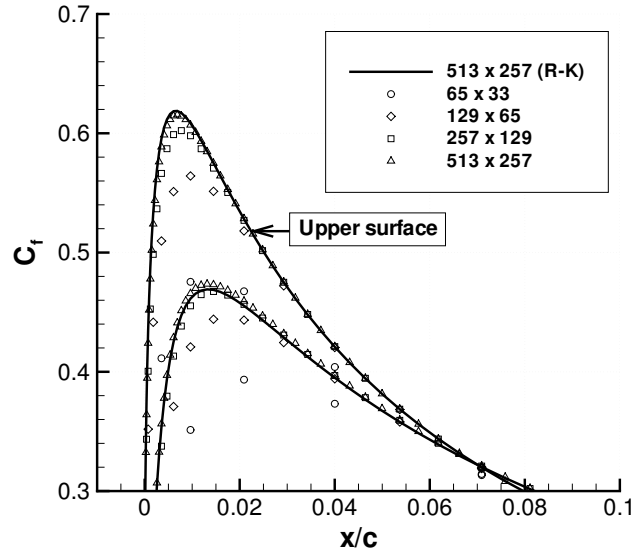
Figure 22: Blowup of Surface skin-friction distribution for laminar over lifting Kármán-Trefftz airfoil ($\alpha = 2°$, $Re_c = 200$).
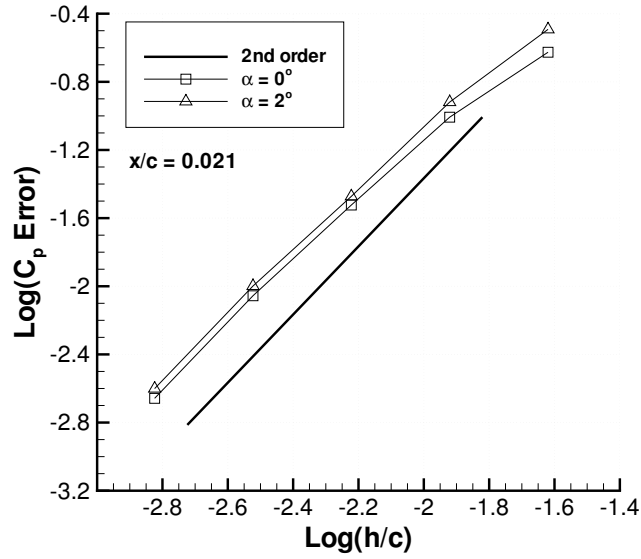
Figure 23: Variation in pressure coefficient error with mesh refinement for laminar flow over Kármán-Trefftz airfoil. Mesh sequence: $33 \times 17 \rightarrow 513 \times 257$; $x/c = 0.021$; $\alpha = 0°, 2°$; $Re_c = 200$.
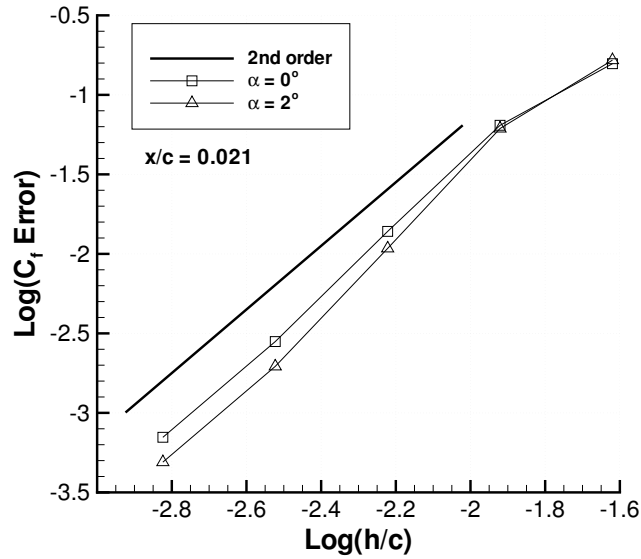
Figure 24: Variation in skin-friction coefficient error with mesh refinement for laminar flow over Kármán-Trefftz airfoil. Mesh sequence: $33 \times 17 \rightarrow 513 \times 257$; $x/c = 0.021$; $\alpha = 0°, 2°$; $Re_c = 200$.
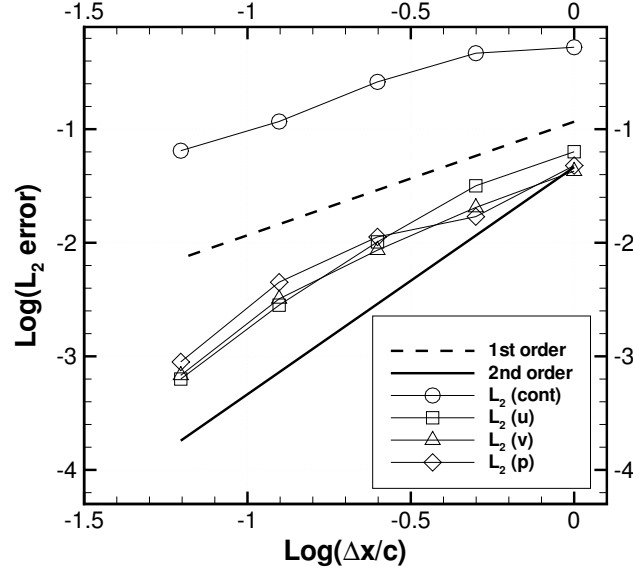
Figure 25: Behavior of error in u, v, p, and continuity with mesh refinement for laminar flow over Kármán-Trefftz airfoil. Mesh sequence: $17 \times 9 \rightarrow 257 \times 129$; $\alpha = 0°$; $Re_c = 200$.
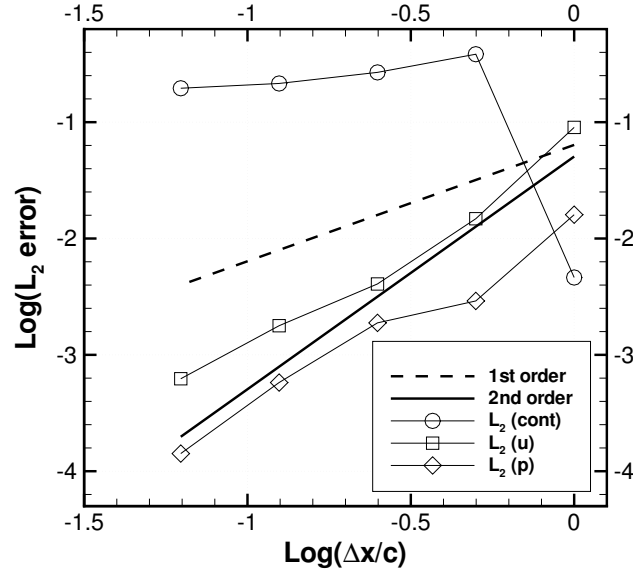
Figure 26: Wake line behavior of L_2 error in u, p, and continuity with mesh refinement for laminar flow over Kármán-Trefftz airfoil. Mesh sequence: $17 \times 9 \rightarrow 257 \times 129$; $\alpha = 0°$; $Re_c = 200$.

36
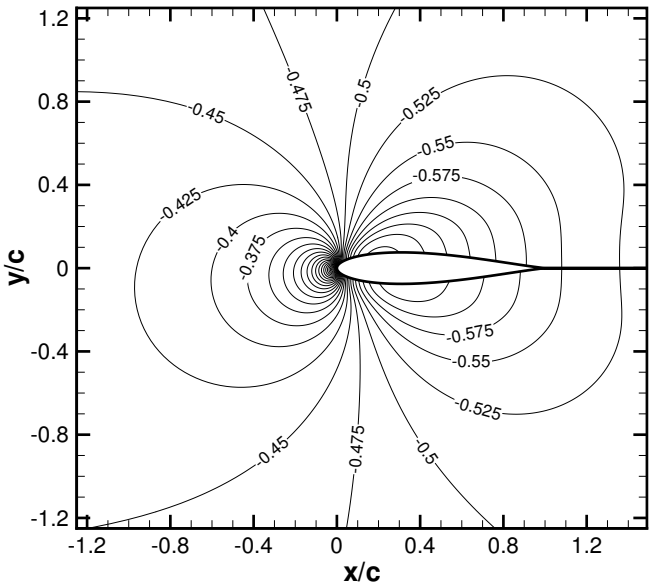
Figure 27: Pressure contours for laminar flow over lifting Kármán-Trefftz airfoil ($\alpha = 2°$, $Re_c = 200$).
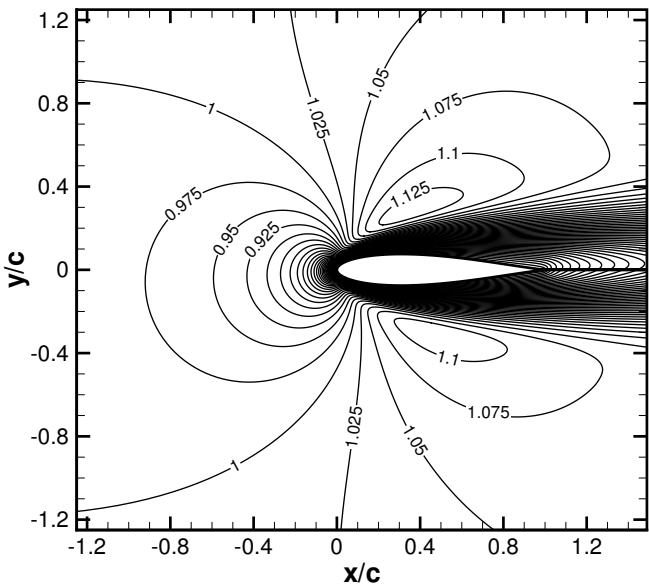
Figure 28: Velocity contours for laminar flow over lifting Kármán-Trefftz airfoil ($\alpha = 2°$, $Re_c = 200$).
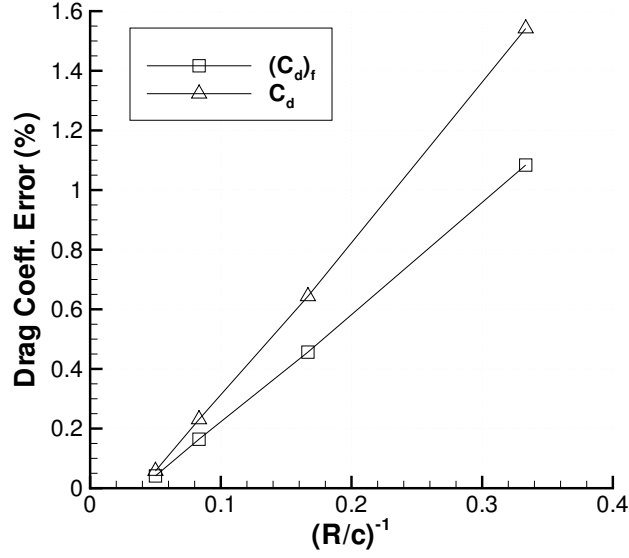
Figure 29: Error in skin-friction and total drag coefficient due to outer boundary location (Kármán-Trefftz airfoil, $\alpha = 0°$, $Re_c = 200$).
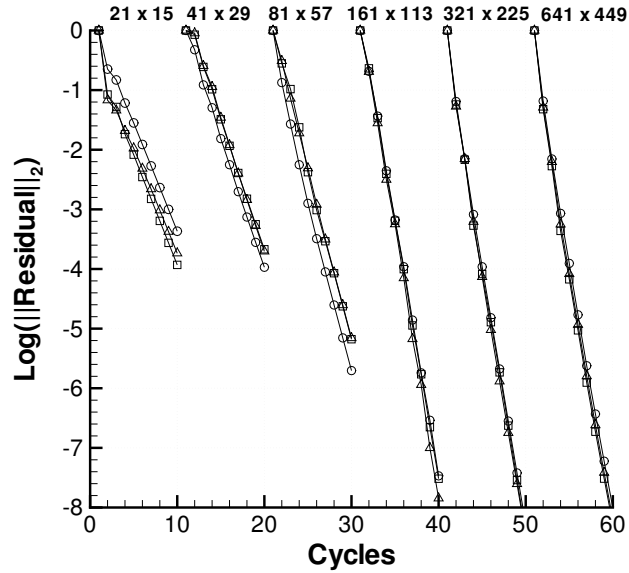
Figure 30: Convergence behavior for laminar flow over nonlifting Kármán-Trefftz airfoil ($\alpha = 0°$, $Re_c = 200$, OB = 20 chords). Residual symbols: Circle for pressure, square for x-momentum, triangle for y-momentum.
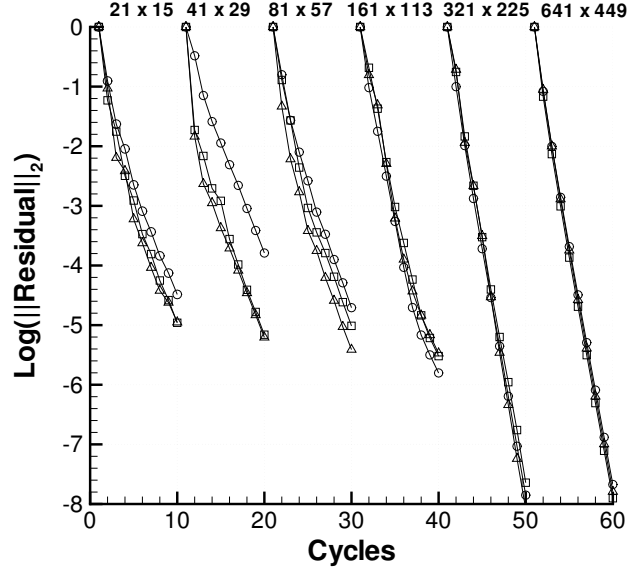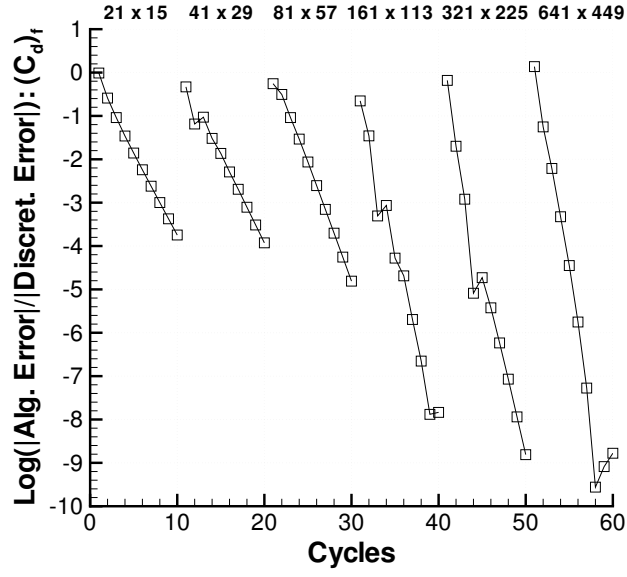
Figure 31: Convergence behavior for laminar flow over nonlifting Kármán-Trefftz airfoil ($\alpha = 0°$, $Re_c = 600$, OB = 20 chords). Residual symbols: Circle for pressure, square for x-momentum, triangle for y-momentum.
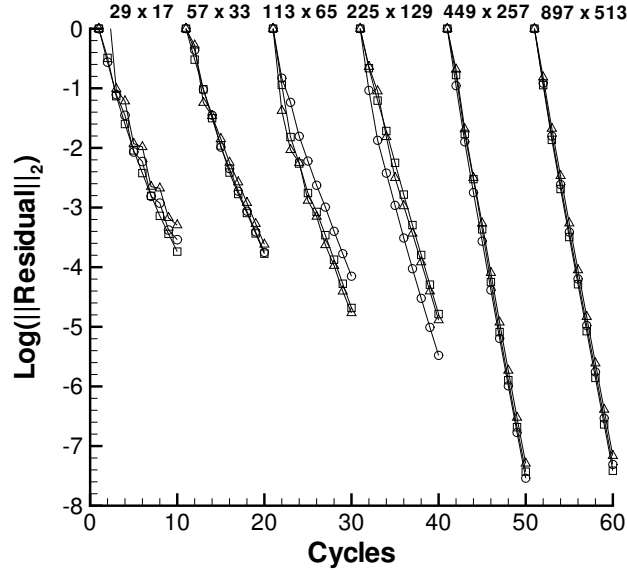
Figure 32: Convergence behavior for laminar flow over nonlifting Kármán-Trefftz airfoil ($\alpha = 0°$, $Re_c = 600$, OB = 20 chords). Residual symbols: Circle for pressure, square for x-momentum, triangle for y-momentum.

Figure 33: Convergence behavior of skin-friction drag coefficient for laminar flow over Kármán-Trefftz airfoil ($\alpha = 0°$, $Re_c = 200$, OB = 20 chords).

REPORT DOCUMENTATION PAGE

Form Approved
OMB No. 0704-0188

1. REPORT DATE *(DD-MM-YYYY)*	2. REPORT TYPE	3. DATES COVERED *(From - To)*
01- 05 - 2004	Technical Memorandum	

4. TITLE AND SUBTITLE

Evaluation of a Multigrid Scheme for the Incompressible Navier-Stokes Equations

5a. CONTRACT NUMBER

5b. GRANT NUMBER

5c. PROGRAM ELEMENT NUMBER

6. AUTHOR(S)

Swanson, R. C.

5d. PROJECT NUMBER

5e. TASK NUMBER

5f. WORK UNIT NUMBER

23-762-45-CA

7. PERFORMING ORGANIZATION NAME(S) AND ADDRESS(ES)

NASA Langley Research Center
Hampton, VA 23681-2199

8. PERFORMING ORGANIZATION REPORT NUMBER

L-18375

9. SPONSORING/MONITORING AGENCY NAME(S) AND ADDRESS(ES)

National Aeronautics and Space Administration
Washington, DC 20546-0001

10. SPONSOR/MONITOR'S ACRONYM(S)

NASA

11. SPONSOR/MONITOR'S REPORT NUMBER(S)

NASA/TM-2004-213026

12. DISTRIBUTION/AVAILABILITY STATEMENT

Unclassified - Unlimited
Subject Category 02
Availability: NASA CASI (301) 621-0390   Distribution: Standard

13. SUPPLEMENTARY NOTES

An electronic version can be found at http://techreports.larc.nasa.gov/ltrs/ or http://ntrs.nasa.gov

14. ABSTRACT

A fast multigrid solver for the steady, incompressible Navier-Stokes equations is presented. The multigrid solver is based upon a factorizable discrete scheme for the velocity-pressure form of the Navier-Stokes equations. This scheme correctly distinguishes between the advection-diffusion and elliptic parts of the operator, allowing efficient smoothers to be constructed. To evaluate the multigrid algorithm, solutions are computed for flow over a flat plate, parabola, and a Karman-Trefftz airfoil. Both nonlifting and lifting airfoil flows are considered, with a Reynolds number range of 200 to 800. Convergence and accuracy of the algorithm are discussed. Using Gauss-Seidel line relaxation in alternating directions, multigrid convergence behavior approaching that of O(N) methods is achieved. The computational efficiency of the numerical scheme is compared with that of Runge-Kutta and implicit upwind based multigrid methods.

15. SUBJECT TERMS

Multigrid; Navier-Stokes; Incompressible; Airfoil

16. SECURITY CLASSIFICATION OF:			17. LIMITATION OF ABSTRACT	18. NUMBER OF PAGES	19a. NAME OF RESPONSIBLE PERSON
a. REPORT	b. ABSTRACT	c. THIS PAGE			STI Help Desk (email: help@sti.nasa.gov)
U	U	U	UU	47	19b. TELEPHONE NUMBER *(Include area code)* (301) 621-0390

Standard Form 298 (Rev. 8-98)
Prescribed by ANSI Std. Z39.18